Journal of Power Sources 195 (2010) 7856–7879

Contents lists available at ScienceDirect

Journal of Power Sources

journal homepage: www.elsevier.com/locate/jpowsour

Review

# Application of XPS to study electrocatalysts for fuel cells

C.J. Corcoran[a], H. Tavassol[a], M.A. Rigsby[a], P.S. Bagus[b,*], A. Wieckowski[a,*]

[a] Department of Chemistry, University of Illinois at Urbana-Champaign, Urbana, IL 61801, United States
[b] Center for Advanced Scientific Computing and Modeling (CASCaM) and Department of Chemistry, University of North Texas, Denton, TX 76203, United States

ARTICLE INFO

*Article history:*
Received 9 April 2010
Received in revised form 3 June 2010
Accepted 4 June 2010
Available online 11 June 2010

*Keywords:*
X-ray photoelectron spectroscopy
Fuel cells
Catalysts
Synchrotron
Nanoparticle
Biofuel cell

ABSTRACT

Analysis of the surface is paramount to understanding the reactivity, selectivity, and catalytic ability of substances. In particular, this understanding is required to make an efficient use of the catalytic surfaces in fuel cells. X-ray photoelectron spectroscopy (XPS) allows determination of changes in the electronic structure for different surface preparation and composition based, mainly, on shifts of the binding energies of core-level electrons. It is also an ideal method that allows identification of the surface or near surface species in relation to fuel cell catalysis. However, the fundamental theoretical concepts, which are used to analyze and interpret XPS spectra are sometimes not correctly understood or correctly applied. In this review, we not only report on XPS operational parameters in use for fuel cell electrocatalysis, but, more significantly, we review and provide rigorous definitions of fundamental concepts used to understand XPS spectra, including the separation of initial and final state effects and the relaxation of valence electrons to screen core-holes. An additional direction of our review is to show the relationships between XPS binding energy shifts and XPS satellite structure with chemical bonding and chemical interactions. However, our primary concern is to provide reviews of representative cases of the application of XPS to solving fuel cell and electrocatalysis-related problems, highlighting progress in this laboratory. We begin with descriptions of essential issues in fuel cell science and with a review of key concepts of XPS. Then, we briefly report on the XPS instrumentation, after which, studies of fundamental importance to electrochemical processes are reviewed. This review includes an overview of complex organic and biological systems in relation to fuel cell electrocatalysis (probed via XPS). We conclude with a discussion of modern developments in XPS methodology.



**Contents**



* Corresponding authors.
*E-mail address:* andrzej@scs.illinois.edu (A. Wieckowski).

0378-7753/$ – see front matter © 2010 Elsevier B.V. All rights reserved.
doi:10.1016/j.jpowsour.2010.06.018

## 1. Introduction

### 1.1. Fuel cells

Fuel cells are attracting considerable attention as a means of producing electrical energy through the oxidation of small molecules. The technology is more efficient than conventional power sources, and can provide cleaner and cheaper energy, depending on the chosen fuel. Polymer electrolyte membrane fuel cells, also known as proton exchange membrane (PEM) fuel cells, utilize hydrogen as a fuel. Direct methanol fuel cells (DMFCs) have methanol as the energy source. Additional information concerning these and other fuel cells can be found in Refs. [1,2]. In order for fuel cells to become a viable alternative to our traditional energy infrastructure, certain shortcomings of the technology must be overcome. Platinum catalysts are widely regarded as the best electrodes for most fuel cell applications, but their use, as well as other platinum group metals, has several limitations, which include price, reserve amount, reactivity and selectivity, and loss of catalytic efficiency over time as a result of poisoning [3,4]. Therefore, for economical purposes, noble metal-based fuel cells need to use significantly less noble metal components than what is currently utilized, and/or catalysts must be created from cheaper and more available materials.

Research into fuel cell catalysis has focused primarily on increasing catalytic efficiency and reducing poisoning. In both cases, enhanced activity has been achieved through alloying a second metal to platinum. Bimetallic catalysts have been studied extensively and it has been shown that they reduce or eliminate the limitations described above. Their enhanced activity can be attributed to the bifunctional mechanism as well as structure or electronic effects [5]. Of these contributions, electronic effects remain poorly understood and, hence, are now receiving much attention. Nørskov et al. developed a model employing first-principle DFT calculations that can predict the chemisorption energy of poisoning or reactive intermediates such as carbon monoxide or hydrogen adsorbed on various transition metal and bimetallic surfaces [6–8]. These calculations involve the interaction of adsorbate molecular orbitals with the transition metal surface sp and d bands. It was suggested that changes in adsorption energies and activation barriers for reaction can be correlated to changes in the position of the center of the metal/alloy d-band with respect to the Fermi level. In particular, the strength of the bonding of an adsorbate to a metal surface has been related to the position of the center of the d-band. The farther away the d band center is from the Fermi level, the weaker the bonding. In other words, the surface electronic structure of an alloy can be altered by lattice strain [9,10] as well as by transfer of charge between the two metals [11,12]. Nørskov's d-band center theory suggests that these effects lead to a narrowing or widening of the d-band and a subsequent shift in its center of gravity towards or away from the Femi level (in order to maintain a constant filling of the d-band). Shifts in the d-band center position correspond to shifts in electron core-level binding energies, allowing for the use of X-ray photoelectron spectroscopy (XPS) to measure the density of electronic states of the metallic catalyst. For example, in terms of the commonly used Pt-Ru catalytic systems, addition of Ru causes the Pt lattice to compress, which downshifts the d-band center with respect to the Fermi level [13]. This results in weaker adsorption bonds between the metal surface and CO adsorbate that may make the initial step of CO electrooxidation easier.

### 1.2. X-ray photoelectron spectroscopy (XPS)

XPS, also known as electron spectroscopy for chemical analysis (ESCA) [14,15], is a technique oftentimes employed in studying heterogeneous catalysts. The technique measures core-level binding energies (BEs) of ejected photoelectrons from atoms at or near the surface of a catalyst sample. In addition to XPS, another core-level spectroscopy is X-ray absorption spectroscopy, or XAS. While XPS provides information about occupied states of a system, XAS provides information about unoccupied states. Because these unoccupied states are over a broad range of energy, the theoretical interpretation of XAS is more complex than for XPS. For this reason, an overview of XAS is outside the scope of the present review. For further information about XAS, we refer the reader to an excellent book by Stöhr [16]. An application of an electron loss spectroscopy that is an analogue of XAS has been made by Mrozek et al. [17,18] to study sulfate adsorption on Au electrodes and the interested reader is referred to this work.

On one level, XPS can be used as an analytical tool since information on peak heights, relative binding energies (BE's), and peak areas allows the identification of the elements and compounds present at or near the surface and provides estimates of their relative concentration. XPS can also achieve variable depth sensitivity either through angle-resolved photoemission [19] or by tuning the photon energy for greater or smaller electron mean free paths with

synchrotron radiation [20]. On another level, XPS BE's and BE shifts, ΔBE's, as well as XPS satellite structure reflect the chemical and electronic states of atoms of the core-ionized atoms. Properly interpreted, BE shifts provide the materials information [21–28] that is required to understand and predict a material's catalytic properties. Most XPS measurements are carried out in ultra-high vacuum (UHV) environments, which is not the environment appropriate to electrochemical processes. However, with the advent of ambient pressure XPS, discussed in Section 6.2, samples may be probed at gas pressures as high as 5–10 Torr [29,30].

## 2. Fundamentals of XPS

### 2.1. The photoelectric effect

The fundamental relationship for the photoelectric effect, as originally set forth by Einstein in 1905, is the basis for the XPS technique [31]:

$$KE = h\upsilon - BE^F \quad (1a)$$

where $h\upsilon$ is the energy of the incident photon, KE is the kinetic energy of the photoelectron, and $BE^F$ is the binding energy, BE, of the ejected photoelectron where the ionized target is left in a state labeled F. As we discuss later, there may be several final states corresponding to the removal of an electron from a particular shell of the system. In a photoemission experiment, one knows the incident photon energy, measures the kinetic energy of the photoelectron, and deduces the $BE^F$ through Eqs. (1a) and (1b). The intensity, $I^F$, of the photoelectrons with $BE^F$ are also measured; in general, one is normally concerned with relative, as opposed to absolute, intensities and it is customary to use the notations $I_{rel}$ or $I$(rel). The principle objective of photoelectron spectroscopies is to use the measured values of $I$ and BE to obtain information about the chemical composition and the chemical bonding of the system that is studied. An important theme of our review is that the combination of theoretical studies with experimental measurements greatly aids in the interpretation of the chemical meaning and chemical significance of the features of the photoemission spectra.

It is common to distinguish between ultra-violet photoemission spectroscopy, UPS, and XPS. The photon energies for UPS are from the decay of excited states of HeI, $h\upsilon = 21$ eV, and from the decay of HeII, $h\upsilon = 41$ eV. The photon energies for laboratory XPS are normally from either Mg $K_\alpha$ radiation with $h\upsilon = 1254$ eV or Al $K_\alpha$ with $h\upsilon = 1486$ eV. However, the availability of synchrotron radiation where photon energies are available over a wide range of energy, see, for example, Ref. [32], blurs a distinction based on photon energy. It is better to view UPS as probing valence levels that may be directly involved in chemical interactions and XPS as probing core-levels, where the deeper core-levels are not involved, at all, in chemical interactions. The advantage of UPS is precisely that the BE's of bonding levels are measured and one hopes to infer information about the chemical bonding from the number of the valence levels and from their relative energies. An important disadvantage of UPS is, however, that the spectra are typically quite complex because of the large number of valence levels; furthermore, intuitive explanations of valence level BE shifts in terms of bonding properties may be misleading [33,34]. On the other hand, XPS spectra are much simpler with one or a few peaks observed for the ionization of a given core-level; furthermore, the position, the relative intensities, and even the number of these features can be related to the nature of the chemical environment of the core ionized atom [14,15,35–37]. This is the reason that the name ESCA, Electron Spectroscopy for Chemical Analysis [14,15], is often used to describe XPS. In the simplest terms, the elemental composition of a material can be identified by the presence or absence of core lines in the XPS and the intensities of these lines indicate approximately [38] the stoichiometry of the composition. However, detailed analyses of BE shifts [23,35] and of the satellite structure [36,37,39] do provide direct information about the chemistry of the material being studied.

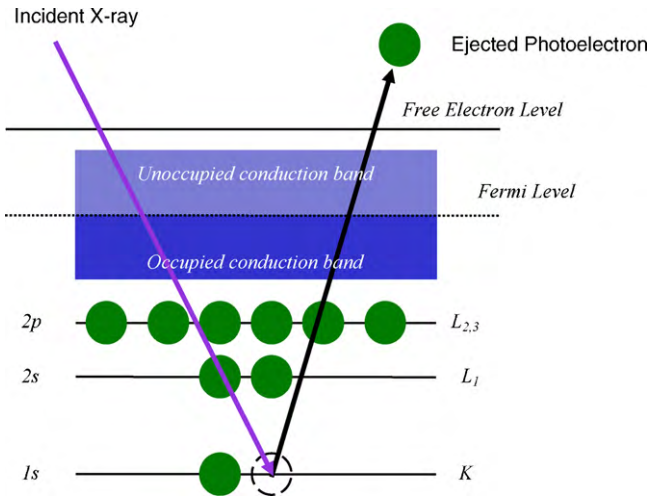


**Fig. 1.** Schematic view of the photoelectron emission process. An incident X-ray photon is absorbed and a photoelectron is emitted; in the example shown from the 1s, or K, shell. Measurement of its kinetic energy allows one to determine the BE of ionized electron; see text.

A schematic view of the photoemission process for a core-level electron in a solid is shown in Fig. 1. The schematic shows removal of a 1s electron. The figure also introduces notations commonly used in XPS. For the metal sample in Fig. 1, the Fermi level, $E_F$, is shown dividing the occupied and unoccupied regions of a metal conduction band. For a clean metal surface, there is an interface dipole that an electron must cross before it leaves the solid sample; this interface dipole modifies, i.e., lowers, the kinetic energy of the photoelectron [40] and must be taken into account with an additional term in Eq. (1a), see below. This figure also shows the nomenclature used for the core-levels that are ionized. Since they are not involved in the chemical bonding or the chemical interactions of the system, these core-levels are labeled using atomic notation. Thus, the lowest, most strongly bound level is a 1s level or, in X-ray notation, a K level. The next shell, the L shell, includes the 2s, or $L_1$ sub-shell, and the spin-orbit split 2p sub-shell with $2p_{1/2}$ and $2p_{3/2}$, or $L_2$ and $L_3$, levels; the spin-orbit splitting is not shown in the figure. Following photoemission, the system is left in a highly excited state that decays through one of two processes [41]: an X-ray photon is emitted, a process known as X-ray fluorescence; or an Auger decay may occur where one electron fills the core-hole and another electron is emitted with a kinetic energy that conserves the total energy.

The relationship of Eq. (1a) is rigorously valid only for measurements in the gas phase. For measurements of condensed phase systems, there are additional considerations and additional potentials for investigating the structure of the matter. A relatively minor fact involves the zero of the BE determined. An additional term is required in Eq. (1a) to take into account the work functions of the sample and the spectrometer, $\Phi_{spec}$ [31,41].

$$BE^F = h\upsilon - KE - \Phi_{spec} \quad (1b)$$

However, this mainly affects the absolute value of the BE. It is a standard procedure to reference the XPS spectra data to the Fermi level, $E_F$, of the sample rather than to vacuum as is done in gas phase XPS. However the relative BE's of different XPS peaks are not affected by this choice of zero. For condensed systems, XPS is surface sensitive because photoelectrons may be inelastically

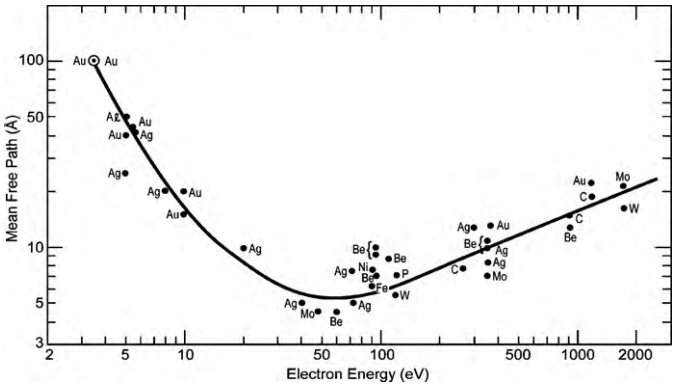


**Fig. 2.** The mean free path of electrons in different solids as a function of the kinetic energy of the electrons. Ref. [44] (with permission).

scattered as they escape across the surface to be detected by the spectrometer [31,41,42]. Thus photoelectrons that are created at or near the surface will have a smaller possibility for inelastic collisions before they exit the sample while electrons that are created deep within the material have a much greater probability of being scattered. The important parameter to determine the depth that is sampled by XPS is the inelastic mean free path, IMFP; the distance where 1/e of the electrons in a beam have suffered an inelastic collision [43]. The curve of IMFP as a function of the electron energy for several different metals, see Fig. 2 taken from Ref. [44], shows that the mean free path is not strongly dependent on the material, but that it is strongly dependent on the electron energy–with the shortest IMFP of ~5 Å at ~50–100 eV electron energy. Thus, it is possible to tune the surface sensitivity of a measurement by using photon energies of 50–100 eV above the BE of a given core-level [45]; however, this tuning requires the use of synchrotron radiation. Further, to probe more of the surface in XPS experiments, one may vary the angle with respect to the surface at which the electrons are detected; electrons exiting along the surface normal may come from a deeper distance within the bulk, while electrons at grazing-emission angles come mostly from the upper surface layers [19].

A problem of special importance for XPS from condensed systems arises from the background of electrons that have suffered inelastic losses. Electrons that have undergone inelastic losses will have a lower kinetic energy and, hence from Eq. (1b), will appear to have been ejected from states with a higher BE. In particular, the background can give misleading information about the intensity of electrons ejected from more strongly bound final states. In order to have a more accurate representation of the XPS spectrum, the contribution of the inelastically scattered electrons can be removed by subtracting an estimate of the background due to these scattered electrons. One method for estimating the background comes from Shirley [46] and another method comes from Tougaard [47,48]. While a detailed analysis of these background subtraction methods is beyond the scope of this review, we present in Fig. 3 an XPS spectrum showing the importance of this correction [46]. The figure shows two photoelectron spectra for the valence band of Au; the upper spectrum is before and the lower spectrum is after background removal. In the uncorrected spectrum, the high BE limit (low channel number) is ~8000 counts greater than the low BE limit at $E_F$. Once the background correction is made, the two limits are at the same number of counts. An important point to note is that the background corrections are significant; in this case, it is ~25% of the intensity maxima. Furthermore, the corrections are not quite unique and depend, to a greater or lesser extent, on the choice of parameters chosen for the subtraction.

A representative XPS scan over 1 keV BE is shown in Fig. 4 for a submonolayer of Pt spontaneously deposited on a Rh(1 1 1) single crystal; this spectrum was taken with our electrochemical XPS

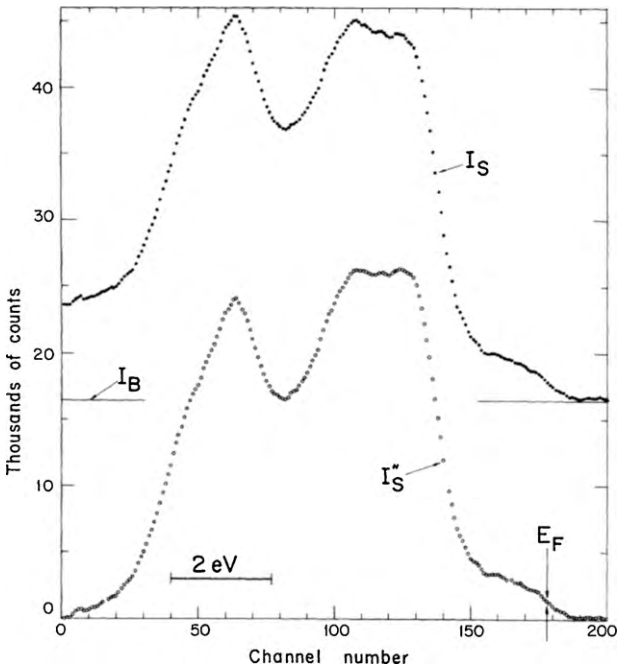


**Fig. 3.** XPS spectra of the gold valence bands before and after corrections for background and scattering. In the raw, uncorrected spectrum, the high BE limit (low channel number) is ~8000 counts greater than the low BE limit at $E_F$. Upon correction, the two limits are at the same number of counts. Ref. [46] (with permission).

system [49]. There is clearly a large uncorrected background of low kinetic energy. The importance (and the need) of background subtraction to permit quantitative analysis of spectral intensities is clear. This figure shows two of the three observable properties of XPS: the BE and the $I_{rel}$. The doublet at ~300 eV is the spin-orbit split $3d_{3/2}$ and $3d_{5/2}$ peaks, where the $3d_{3/2}$ is ~10 eV higher in BE than the $3d_{5/2}$. To a first approximation, neglecting many-body effects, the relative intensities of the XPS peaks within a given sub-shell are given by the number of electrons in the ionized sub-shell [50,51]. Thus, the $I_{rel}$ of the $3d_{5/2}$ and $3d_{3/2}$ should be 3:2. Between different sub-shells and different shells, the photoelectric cross-section depends strongly on the particular shell, which, in addition to the occupation of the shell, determines the $I_{rel}$ of XPS peaks. Furthermore, these cross-sections also depend on the photon energy [52,53]. In particular, the tabulation of cross-sections by Yeh and Lindau [53] provides an excellent guide to lines that may be readily measured for the XPS of particular elements. For the theoretical determination of $I_{rel}$, the sudden approximation, SA,

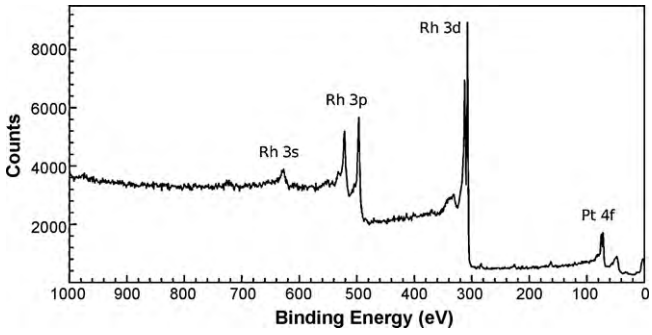


**Fig. 4.** A wide-range XPS spectrum of platinum spontaneously deposited on rhodium(1 1 1). Listed are the Pt 4f (~70 eV), Rh 3d (~300 eV), Rh 3p (~500 eV), and Rh 3s (~630 eV). Because such a small amount of Pt is present, Pt 4d (~320 eV), 4p (~520 and ~610 eV), and 4s (~725 eV) peaks are difficult to observe. The Pt 4d peaks are mixed into the Rh 3d peaks making differentiation between the two sets of peaks difficult. Ref. [49].

developed for XPS by Aberg, is commonly used [51,54,55]. The SA is rigorously correct in the limit of infinite photon energies, but it is accurate for the photon energies normally used for XPS measurements [51]. An important value of the SA $I_{rel}$ is to be able to theoretically determine the intensities of main XPS peaks and of many-body satellites.

### 2.2. Fundamental concepts in XPS

We describe below the fundamental concepts and terms that provide the context in which the key properties of XPS features are understood and are related to the chemical bonding and chemical interactions in the material studied. This is important because it provides the basis for understanding XPS spectra and for understanding how different features arise. It is also important because sometimes these concepts are not clearly understood and there may be misunderstandings connected with their use. We will also consider here descriptions of different kinds of many-body effects that may, and often do, lead to complex and intense satellite structures in addition to the main peaks. Finally, we consider briefly the theoretical models that we have used to aid in the interpretation of the XPS BE shifts and many-body satellites [21,23,25,28,36,37,39]. Our intent here is to present and to clarify the basic chemical and physical ideas; we refer the reader to earlier publications for the mathematical details of these expressions; see Refs. [35,36] and references therein.

We consider first the distinction of initial state and final state effects for the absolute and relative values of BE's. There are two very important and closely related concepts, namely Koopmans' theorem, KT, BE's and the relaxation energy, $E_R$, that must be added to the KT BE's to give correct absolute values for the BE's. The relaxation energy arises from a process often described as screening of the core-hole. In particular, the concept of an equivalent core atom to replace the core ionized atom, due to Jolly [56], provides a useful way to understand relaxation and screening. An initial state effect is the value of the BE of a given core-level electron when the electron is removed but all the other electrons, the passive electrons, remain in states identical to their original configuration before core-level ionization. In terms of an orbital description, this means that the orbitals are kept fixed and only the occupation of the ionized shell is reduced by 1. This is rigorously a frozen orbital, FO, approximation, which may be computed within Hartree-Fock, HF, or Density Functional Theory, DFT. Within HF theory, this frozen orbital BE is given by $-\varepsilon_i$, the orbital energy of the ionized electron. This is referred to as Koopmans' theorem since was originally shown for closed-shell systems by Koopmans. For open shells, the meaning of the KT BE must be modified slightly to take account of the coupling of the open core-shell with the open valence-shell [51]. The value of FO or KT BE's is that they directly reflect and measure the potential at the core of the ionized atom due to the valence and conduction band electrons that surround the ionized atom; hence they provide insight into the chemical environment and chemical bonding of the atom that has been ionized. However, because the KT BE's neglect final state relaxation and screening effects, they provide rather poor values for the absolute values of core-level BE's, as we discuss below. Before we turn to these final state effects, it is worth noting that, within DFT, the negative of the Kohn-Sham orbital energy, $-\varepsilon_i$(KS), does not give the FO or KT BE. Indeed, $-\varepsilon_i$(KS) is an approximation to the fully relaxed BE [57].

It is possible to take what are described as final state effects on the BE's into account by calculating two solutions to the variational equations, either HF or KS. The first solution is for the state where all the core-levels are filled, described as the initial state, and the second solution is for the state where an electron has been removed from one of the occupied levels, described as the final state. Following the initial work of Bagus [58], one then computes the ΔSCF BE as:

$$\mathrm{BE}(\Delta\mathrm{SCF}) = E(\text{final state}) - E(\text{initial state}) \quad (2a)$$

where $E$(final state) and $E$(initial state) are the total energies for the ionized and unionized states, respectively. Indeed, the BE(ΔSCF), computed either with HF or DFT, give reasonable approximations to observed BE's for many systems; see, for example, Refs. [50,58–60]. For molecular and condensed systems, it is common to consider vertical transitions where the same geometries are used for the two states because the XPS ionization is on a much shorter time scale than the nuclear motion. However, it is possible to take nuclear motion into account [59] and it has been shown that this may lead to a Franck-Condon broadening of the XPS lines. The difference between the FO or KT BE and the ΔSCF BE is the relaxation energy, $E_R$,

$$E_R = \mathrm{BE(KT)} - \mathrm{BE}(\Delta\mathrm{SCF}) \geq 0 \quad (2b)$$

The relaxation energy arises because the passive orbitals relax or respond to the presence of the core-hole; the variational principle assures that $E_R > 0$. The equivalent core analysis [56] provides a way to understand, in chemical terms, the $E_R$ and the changes of the passive orbitals due to the core-hole. As far as the outer, or valence, electrons are concerned, the atom with a core-hole is, to a good approximation, the same as an atom with a nuclear charge larger by 1, denoted as $Z+1$. In effect, if we make a 1s hole on an O atom, this appears to be like $F^+$ and if we make a 4d hole on a Pt atom, this appears to the remainder of a nanoparticle, for example, to be an $Ag^+$ impurity. For an isolated atom, the response or relaxation of the passive orbitals is a contraction of the orbitals in response to the larger effective charge, $Z+1$, that these electrons experience. For a compound, there is an additional, extra-atomic, response to the core-hole because of the presence of an impurity ion with charge $Z+1$; see, for example, Ref. [61] for a discussion of extra-atomic relaxation. This relaxation is commonly described as a screening of the core-hole since valence and conduction band electrons move toward the $Z+1$ impurity to screen, or damp out, the electric field due to the $Z+1$ "impurity", core-ionized atom. The sum of the atomic and extra-atomic screening can be quite large, easily amounting to 20–50 eV, depending on the core-hole and the element that is ionized. This is why the KT BE's are very poor approximations to the absolute values of the BE's. However, as we discuss below, an important concern is for the shifts of BE's for inequivalent atoms in a compound or for atoms in different compounds of comparable size. It can be shown that, in these cases, the BE shifts are dominated by the initial state effects. In other words, while the $E_R$ values are very large, the differences in the $E_R$ for different atoms are, for the cases described above, rather small, even for cases where there is a systematic increase of the size of a system. Furthermore, even when the $E_R$ changes between different systems, initial state effects may still make important contributions to the BE shifts between systems. An example of interest for our electrochemical studies is for BE shifts of nanoparticles with increasing particle size, where it is clear the $E_R$ increases with increasing particle size. Here, rigorous analyses show that initial state effects do make important contributions to the shift of BE's with increasing particle size [10,23,28].

For the discussion above, separation into initial and final state effects was related to knowledge of BE(KT), a quantity that is available only from theoretical studies. However, from reasonable assumptions about the nature of atomic and extra-atomic relaxation, or screening, it is possible to combine measurements of Auger and XPS energies to determine an Auger parameter, [62,63] which allows one to separate initial and final state effects. Specifically, the Auger parameter makes it possible to make this separation for BE shifts, ΔBE. However, caution must be used in selecting the Auger

lines and the photoelectron lines to be combined and for the formulation of the Auger parameter. If proper care is not taken, the Auger parameter can lead to misleading results about the decomposition of BE shifts into initial and final state effects [21].

BE shifts, $\Delta$BE, are commonly used to obtain information about the chemical and electrochemical activity of many catalytic systems, especially nanoparticles [23–25,27,28]. In particular, one wishes to study the BE shifts in the nanoparticles as a function of particle size and of particle composition. A common interpretation of the BE shifts is in terms of the charging, or the effective ionicity of the core-ionized atom. If one ionizes an atom that carries a negative charge with respect to some reference state of the atom, the charge will contribute to a decrease of the BE, while if one ionizes an atom that carries a positive charge, this will contribute to an increase of the BE. However, these relations are often used to deduce the effective charge on an atom through the relationship, $\Delta Q \propto \Delta$BE and this relationship is a serious oversimplification because factors other than the charge on an atom make initial state contributions to the $\Delta$BE; see Refs. [10,21,35] and references therein. These effects include the hybridization of deeper lying valence levels to help the chemical bonding of an atom with its neighbors; this hybridization shifts BE to larger values without charge transfer from the ionized atom. Another effect is the coordination, or the number of nearest neighbors to the ionized atom. When there are more neighbors, there is a contribution to shifts to lower BE's because the environmental charge density surrounding the ionized atom is larger generating an electrostatic potential that lowers BE's. Finally, changes in the mean bond distance may lead to $\Delta$BE because, as well as changing the environmental charge density, the changes in bond distance also lead to changes in the chemical bonding between the atom and its neighbors. The change in "lattice" constant with nanoparticle size is a part of the morphology of particle nucleation and growth and is commonly described as lattice strain. With careful analysis and interpretation of the BE shifts with nanoparticle size, one can better understand the particle growth and possibly also control this growth to obtain desired properties.

A final feature of XPS spectra that we discuss briefly are many-body effects that lead to satellites and that allow these satellites to "steal" intensity from the main XPS peaks. These effects are of special importance for open-shell systems, although the satellites that are described as shake features will also occur for closed-shell systems [38,51,54,64]. We just want to alert the reader to the complications that may be encountered in the analysis of XPS spectra. For open shell systems, multiplet splitting occurs. These peaks come from many-body effects that cannot be described with one electron theory. For example, the closed-shell CO molecule has a single peak at ~300 eV for the C(1s) level and a single peak for O(1s) level at ~ 500 eV. For the NO molecule, which is a radical with a single electron in the $2\pi^*$ level, multiplet splitting leads to doublets for both of the N(1s) and O(1s) peaks. Furthermore, the N(1s) doublet is clearly resolved while the O(1s) doublet has a splitting of ~0.5 eV. This difference in the multiplet splitting infers that the $2\pi^*$ orbital is more predominant on the N atom with only a small fraction of its charge on the O atom. Therefore, understanding the origin of multiplet splitting can provide information about the chemical bonding and the oxidation state of chemical species. The situation can become even more complex when the core shell that is ionized is a spatially degenerate shell and the open shell is a d shell that can involve a large number of angular momentum couplings [36,39,65,66]. Further, many-body effects can arise when there are nearly degenerate sub-shells, as for the 3s, 3p, and 3d shells of the first row transition metal cations. When the open d shell electrons couple high-spin, as in anti-ferromagnetic oxides and fluorides, the near degeneracies of these sub-shells may allow strong mixing of configurations where the electrons have different distributions over the nearly degenerate sub-shells. This mixing changes the multiplet splitting and leads to new satellites [67,68]. There are also so-called shake-up and shake-off satellite peaks [54,55]. These satellites can be viewed as the outgoing photoelectron exciting a valence electron to a higher lying bound state or into the continuum leaving behind a more highly ionized state. Because these satellite states have even higher energy than the main core-hole state, the photoelectrons associated with them have a lower kinetic energy. In other words, the BE's of the photoelectrons for the satellite states are larger than for the main core-hole state. In fact, these shake peaks gain intensity because the relaxation or screening of the core leads to a new set of orbitals for the hole state. It is the overlap of the modified hole-state orbitals with the unmodified, or unscreened, ground state orbitals that allows the excited, shake states of the core-hole ion to gain intensity [54]. Indeed, the intensity and the energetic positions of the shake satellites are directly related to the magnitude of the atomic relaxation energy [51,55]. In certain cases, one factor that is important for the intensities and the energies of shake peaks is the degree of covalent bonding of the core-ionized atom. Situations where this consideration is especially important are for ionic compounds [69] and for adsorbates [70]. In these cases, the presence of intense, low-lying satellite peaks in the XPS provide information about the chemical interactions in the system and the chemical state and bonding behavior may be ascertained by analyzing these satellite peaks.

While the experimental methods to be used will be described in the following sub-sections, we indicate here the theoretical methodology that we have used to analyze and provide theoretical analyses of XPS spectra. As materials models, we use clusters of atoms designed to represent nanoparticles and surfaces [10,21,38] and to represent bulk materials [36,38]. For these clusters, we obtain rigorous wavefunctions, where we do not fit parameters whose values are adjusted to fit experimental data. Such fitting to experiment is commonly carried out with semi-empirical methods [71]. However, these empirical adjustments of parameters can lead to misinterpretations and to incorrect assignments [67]. In order to avoid the possibility of such errors, we use formalisms where we do not make empirical adjustments of the parameters in our computations. Thus, if the theoretical results that we obtain do not match the experimental results, we must identify the physical and chemical effects that may have been omitted from the theory or we must identify limitations in the measurements. Details of the methodology and theoretical formulations can be found elsewhere; for non-relativistic calculations see Refs. [38,72] and references therein and for relativistic calculations see Ref. [36] and references therein.

### 2.3. XPS measurements and experimental considerations

XPS spectra are displayed as plots of photoelectron intensity as a function of binding energy or, equivalently, electron kinetic energy; see a typical (survey) XPS spectrum shown in Fig. 4. While it is natural to accurately measure the relative energies of different XPS features, it is less straightforward to obtain absolute values of the XPS BE's [31,41]. The energy scale of the spectrometer used in an instrument is normally calibrated using Au, Ag, and Cu metal standards with XPS peaks of known energy in the energy range of interest for the sample being studied. There are instrumental and inherent factors that broaden the peaks observed in XPS; the broadening is normally characterized as a full width at half-maximum, FWHM. Inherent factors arise from the lifetime of the core-hole states [73] and from Franck-Condon broadening, as discussed in Section 2.2. The instrumental factors include the linewidth of the photon source and the resolution of the electron analyzer. The relative energy resolution of the analyzer, $\Delta E/E$, is the resolving power between $\Delta E$ and kinetic energy $E$ of the peak at which the width is measured. These factors involve either Gaussian or Lorentzian

broadenings and are best fit with a Voigt convolution of Gaussian and Lorentzian broadenings [74]. There is also a background, as discussed in Section 2.2, that arises from the inelastic scattering of the photoelectrons. This background is removed before the XPS peaks are decomposed into broadened contributions from individual final states. Practical methods for background removal are discussed in Refs. [75,76]. Software such as Casa XPS [77] is available for removal of background and for decomposition of the spectra.

XPS is regarded typically to be a non-destructive technique. However, caution should be taken as there are several possible mechanisms for sample damage. X-rays may damage the sample due to thermal effects along with effects from high-energy Bremsstrahlung radiation [31]. In addition to direct chemical effects from the incident radiation, potential problems can also arise from the secondary electrons and photoelectrons from the X-ray source. This is especially true for organic samples [41]. These problems can be remedied by employing a monochromator. The monochromator not only reduces the energy spread of the X-rays, but heat and secondary electrons from the X-ray source are also filtered. An electron flood gun is often used to avoid BE shifts due to the charging of the sample during the XPS measurement [41]. However, the charge-compensating electrons from the flood gun may induce chemical changes in the sample. In addition, damage from the X-ray beam may alter atomic composition, molecular and electronic structure, or the topology of the sample. For experiments requiring long exposure times, it is often practical to monitor the spectra over time for damage. If damage is found, one of the methods to avoid or limit the damage should be employed. These methods include reducing the photon flux or increasing the flux of electrons going into the detector. Sometimes damage cannot be avoided. In such instances, shifting the beam to other areas over time, a technique known as sample rastering, or extrapolating spectra to zero time should be considered.

The primary components of the XPS instrument include the X-ray source, an electron energy analyzer, and the electron detector. The X-ray sources commonly used with a laboratory instrument are Mg Kα (1253.6 eV) and Al Kα (1486.3 eV). These two sources provide at least one core-level for each element in the periodic table, except Hydrogen or Helium. Satellite peaks can appear in a spectrum if a nonmonochromatized X-ray source is used as the excitation source [31,41]. These satellites occur because the main transitions are excited by minor X-rays, which can make spectral assignments more difficult. The X-rays are usually monochromatized to reduce the energy spread of the incident radiation and to produce cleaner spectra. The use of the monochromatized light eliminates satellite lines that originate from a nonmonochromatized X-ray source (see above) and Bremsstrahlung radiation.

The main analyzer present in commercial XPS instruments is the hemispherical sector analyzer (HSA). The HSA is also known as the concentric hemispherical analyzer (CHA) or the spherical sector analyzer (SSA). The electron analyzer and lens are operated in one of two modes to measure electron kinetic energies: constant analyzer energy (CAE) mode and constant retard ratio (CRR) mode. In CAE mode electron kinetic energies are reduced to the same value by the electron lens to maintain a constant energy resolution. The absolute resolution of the spectra is then independent of electron kinetic energy, which is practical for quantitative XPS measurements. As such, this is the chosen method for acquiring XPS spectra. For CRR mode, the method also chosen for Auger experiments, the analyzer retards electrons to some user-defined ratio of their original kinetic energy, resulting in a constant relative resolution.

### 2.3.1. XPS instrumentation for air-sensitive samples

All electrochemical samples (surfaces emerged from electrolytic media) are air-sensitive. Upon exposure to air, sample damage may result from oxidation, force desorption, and/or adsorption of air contaminants to the sample. The methodology for clean, air-free "UHV-electrochemistry experiments" [78] performed in the authors' laboratory has been reported previously [5,26] (Fig. 5). The XPS instrument has electrochemical (EC) and vacuum (UHV) chambers, and hosts a hemispherical sector analyzer (HSA, a part of the ESCA M-Probe by Surface Science Instruments). For the electrochemical experiments, a Teflon sleeve [79] hosts the electrochemical cell compartment where the sample surface is connected to solution via a meniscus. Argon overpressure keeps air effectively out of the chamber. After electrochemical treatment, the cell is removed from the EC chamber and – after closing the small gate valve – the chamber is evacuated down to $\sim 10^{-4}$ Torr with nitrogen sorption pumps. A turbo pump is used to further pump the system down to $10^{-5}$ or $10^{-6}$ Torr. A liquid helium cryopump is

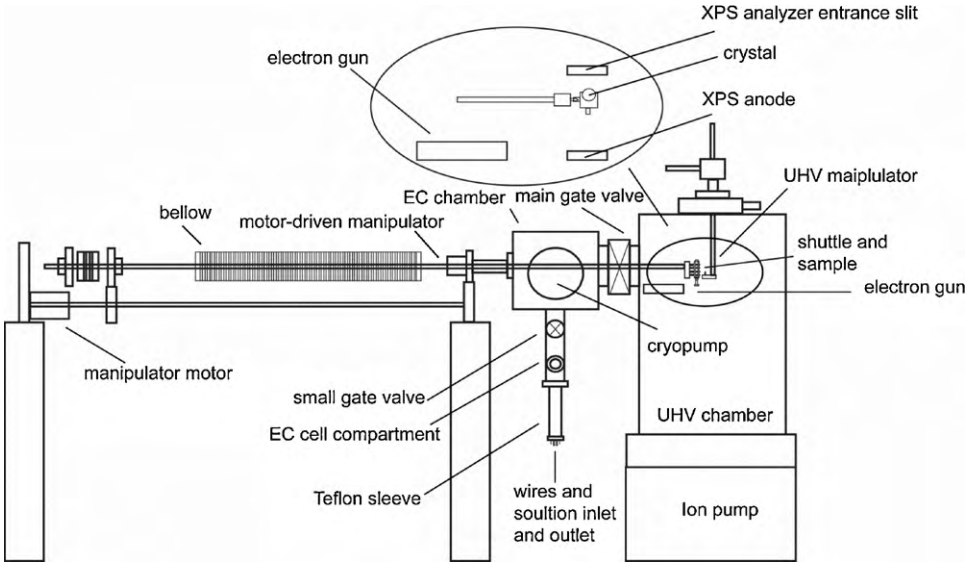


**Fig. 5.** A schematic showing the lateral view of the authors' XPS system. Depicted from right to left: UHV manipulator, UHV chamber, EC chamber, EC cell and motor-driven (horizontal) manipulator with the shuttle and sample (shown inside the UHV chamber). Inset: locking of the shuttle on the UHV manipulator after 90° rotation of the crystal to secure for XPS experiments (notice the 180° rotation versus the demonstrated shuttle position in the UHV chamber). After transferring the shuttle from the horizontal to the UHV manipulator position, the sample surface is at 30° with respect to the analyzer entrance slit (not shown). The angle between the sample surface and the incident X-ray beam is also 30°, and that between the analyzer and the incident X-ray beam is 90°. Ref. [26] (with permission).

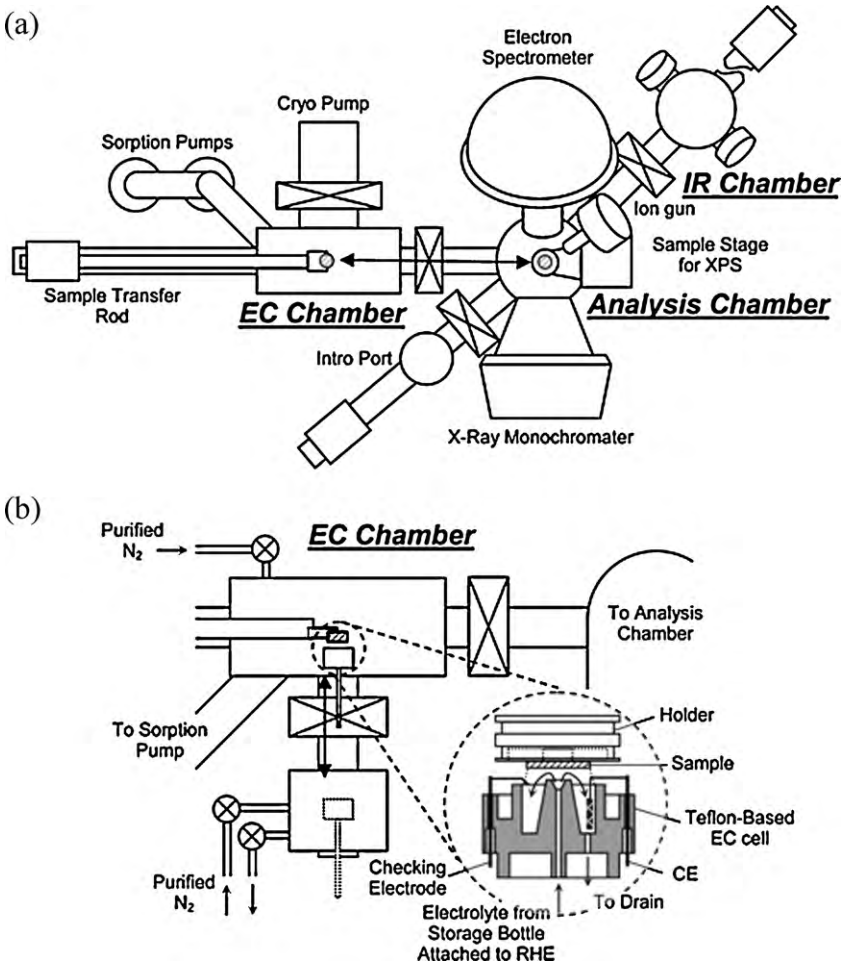


**Fig. 6.** Schematic views of (a) the entire UHV apparatus (top view) and (b) the EC chamber (side view). In the dashed circle, the configuration of an EC cell and a sample electrode is illustrated. The operation of this instrument follows the same procedures mentioned for Fig. 5. Ref. [80] (with permission).

finally used (with the main gate valve still open) as a frontier pump to bring the pressure down to $\sim 10^{-8}$ Torr.

The EC and UHV chambers are connected via the main gate valve (Fig. 5). The sample is transferred between chambers via a motor-driven manipulator while under vacuum. Upon transfer into the UHV chamber, the sample is rotated 90° and positioned below the electron energy analyzer but above the XPS anode (shown in the inset of the figure). The sample surface is at 30° with respect to the analyzer entrance slit (not shown). The angle between the sample surface and the incident X-ray beam is also 30°, and the angle between the analyzer and the incident X-ray beam is 90° (the instrument employs a monochromatic Al Kα line.) After attachment to the UHV manipulator, the motor-driven manipulator is removed and placed into the EC chamber. The main gate valve is then closed, which leads to lowering the pressure in the UHV chamber to ca. $10^{-9}$ Torr. Once this low pressure is achieved, surface characterization is performed using XPS. Argon ion bombardment and annealing (at $3 \times 10^{-8}$ Torr of oxygen for Pt samples) is used to clean/reorder the surface. The ion bombardment/annealing cycle repeats until the appropriate order and cleanliness of the surface is confirmed (by LEED and/or voltammetry). We reiterate that the electrode is routinely transferred between chambers by bringing the EC chamber up to atmospheric pressure with argon. This ensures no damage to the sample from being in contact with air oxygen and atmospheric contaminations.

Another instrument, outlined in Fig. 6 [80] uses a setup similar to the authors' system. The XPS chamber is equipped with a hemispherical electron spectrometer (Model 10-360, PHI), an X-ray source (Model 10-610, PHI), a toroidal monochromator (Model 10-420, PHI), and an ion gun (Model 06-350, PHI) for surface cleaning. The procedure for using this methodology is similar to that described above. A Teflon-based electrochemical cell with a nozzle-like Luggin capillary is in the center, which is connected with an electrolyte solution reservoir through a Teflon tubing (Fig. 6b). The shape of the electrochemical cell allows a rapid solution exchange under a potential control while the electrode is still immersed in the electrolyte.

## 3. Applications of XPS in fundamental studies

### 3.1. Outline

We will report below on fundamental XPS studies of some relevance to electrochemical processes. First, we will begin with a study exploring the structure of water on the Pt(1 1 1) surface. Next we will demonstrate a model system that presents an excellent case study for a strong species interaction with the electrode interface. Afterwards we describe the effects metal particle size has on the electronic structure and catalytic activity of an electrocatalyst. Critical information obtained by XPS on platinum-ruthenium anode electrocatalysts is then discussed followed by the electronic effects observed when depositing metal thin films onto the surfaces of other metals. We conclude with an irreversible deposition study of adspecies on platinum electrodes.

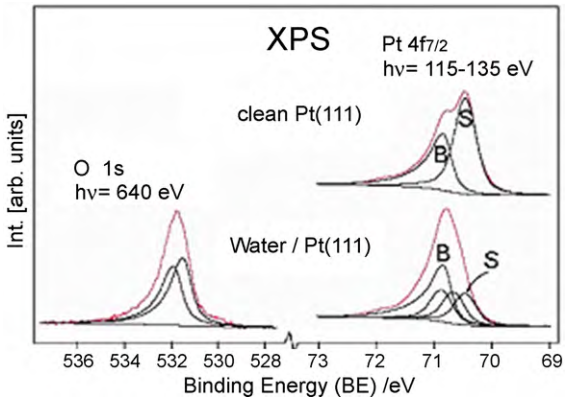


**Fig. 7.** XPS spectra for clean and water covered Pt(1 1 1). The components obtained from a curve fitting analysis, according to the structural model, are shown with solid black lines. (Left) O 1s photoemission spectrum estimated with two separated peaks corresponding to the Pt-O and Pt-HO bonding water molecules. (Right) summed Pt $4f_{7/2}$ spectra taken at three excitation energies (115, 125, and 135 eV) to average out photoelectron diffraction effects (right bottom). Water coordinating to the metal shifts contributions towards the bulk value. All experiments were kept between 100 and 120 K. Ref. [84] (with permission).

### 3.2. Structure and bonding of water on platinum

Interaction of water at the metal surface has been one of the most frequently studied cases studied in gas-phase surface science and is also of relevance to electrochemistry [80–82]. Water molecules are believed to form an adsorbed bilayer [83] where the first layer binds via the oxygen atoms and forms hydrogen bonds to other water molecules. For instance, Ogasawara and co-workers studied adsorption of water on Pt(1 1 1). Density functional theory (DFT) calculations were performed to guide the interpretation of the experimental X-ray absorption, X-ray emission, and XPS data [84]. The synchrotron XPS experiments were performed at a MAX-lab synchrotron facility. A water monolayer was deposited on the surface by annealing a water multilayer at 100 and 120 K, and the amount of water molecules (coordinated to the surface) was determined via the Pt 4f surface core-level XPS shift [61]. For a pure Pt(1 1 1) crystal, the Pt surface atoms were found to have a different BE than the bulk Pt atoms (by 0.4 eV, Fig. 7). Upon exposure to water, the surface atoms were shifted closer to the BE of the bulk atoms. Intensity changes in the peaks indicate that ca. 2/3 of the surface Pt was covered with water. The bilayer model does not account for such a high surface coverage. Further, the computed oxygen 1s BEs for the two water molecules in the bilayer structure have a chemical shift of 1.9 eV. This shift arises if the two layers of water molecules have different screening channels upon core ionization, which is the case for the bilayer model [85] (However, this model-predicted value has not yet been found in the experimental data.) A flat ice layer was determined through computer-modeling for water bonding at the Pt surface. Each water molecule in the flat ice layer possesses three hydrogen bonds to produce a hydrogen bond network. In summary, this study found that water was adsorbed onto the surface nondestructively to form a flat ice layer, where these molecules were bound through alternating metal-oxygen and metal-hydroxyl bonds.

### 3.3. Surface activity of iodine adsorbed at poly- and single-crystalline gold

When iodine is in the surface-bound form, its surface activity causes profound changes in the chemistry of the iodine/iodide redox couple [86]. This system serves as a good case study for a strongly adsorbed and electroactive surface species, and indeed, kinetics of the iodine/iodide (unadsorbed) redox couple can be altered by pre-treating the electrode surface with a full monolayer of iodine [87]. One study compared the surface chemical and electrochemical properties of chemisorbed iodine at polycrystalline gold and on a well-defined Au(1 1 1) single crystal [88]. The oxidative chemisorption and cathodic stripping reductive desorption of iodine were performed on these two Au substrates. Measurements were based on cyclic voltammetry, thin-layer coulometry, XPS, Auger electron spectroscopy (AES), and low-energy electron diffraction (LEED). The Au foils were coated with iodine either by high temperature annealing in a gaseous $N_2$ environment saturated with iodine vapor, or via immersion in 1 mM aqueous KI solution. XPS revealed that the iodine in both preparation methods yielded XPS peaks with BEs: Au $4f_{7/2}$ (84.1 eV) and $4f_{5/2}$ (87.8 eV), and I $3d_{3/2}$ (630.0 eV) and $3d_{5/2}$ (618.4 eV) [88]. Furthermore, no K peaks were observed in the XPS spectra. The Au $4f_{7/2}$ and $4f_{5/2}$ peaks were unchanged after pretreatment with iodine. The results show that iodide was oxidatively adsorbed as zerovalent atomic iodine at potentials between −0.4 V and +0.4 V with respect to the Ag/AgCl reference [88]. Surface iodine was reductively desorbed to aqueous iodide at lower potentials, and was oxidized to iodate at higher potentials.

To acquire more information about the relationship between interfacial structure and adsorbate reactivity, single crystal Au(1 1 1) AES and LEED studies in dilute (1 mM) CsI solution buffered at pH 6.8 were performed. These CsI studies demonstrated ordered adlayer structures at selected potentials. At potentials below −0.4 V (vs. Ag/AgCl), the oxidative deposition potential of iodine, a (4 × 4) quarter-coverage CsI layer was observed. Between −0.4 and −0.2 V, the iodine coverage increased to 0.33. This increase corresponded with a loss of adsorbed Cs atoms. The structure of this adlattice was Au(1 1 1)($\sqrt{3} \times \sqrt{3}$). At potentials greater than −0.2 V, the I coverage reached 0.4 ML. This was accomplished by compression of the original ($\sqrt{3} \times \sqrt{3}$) structure to form an almost hexagonal iodine adlattice with a characteristic ($5 \times \sqrt{3}$) unit cell. With a more positive potential, adsorbed iodine increased until the surface became saturated with a monolayer of close-packed I atoms of the coverage limited by van der Waals forces. Incorporation of additional iodine into this space-limited interfacial layer lead to the formation of molecular $I_2$. From these results, the oxidative chemisorption process can be considered an oxidative underpotential deposition of I atoms on the Au surface while the reductive desorption reaction may be thought of as the cathodic stripping of iodide atoms.

Similar results have been observed for platinum and platinum-based bimetallic systems [26,89–92]. Immersion of platinum into an iodine solution produces an ordered layer of iodine atoms [89]. Further, from XPS measurements, the iodine atoms occupy either threefold hollow sites (619.3 eV) or one-fold atop sites (618.2 eV) [93]. Fig. 8, gives iodine $3d_{5/2}$ XPS spectra for high coverage of iodine on Pt(1 1 1) (a), Pt(1 1 1)/Ru with 0.5 monolayers of Ru (b), and Ru(0 0 0 1) (c). The spectra for (a and b) had a component at 619.4 eV and a component at 618.4 eV: those at a higher BE correspond to iodine in three-fold hollow sites of Pt and the other corresponds to iodine on atop sites. The spectrum in (c) can be fitted with only one component; the shift of 0.3 eV between the higher BE components of (a–b) and (c) can be clearly observed.

Temperature programmed desorption data from Jo and White show that desorption from the atop peak is centered at 650 K and from the three-fold site at 900 K [93]. Later work from Bagus et al. [22] has tried to explain the Pt/I system from theoretical modeling of iodine atoms on platinum clusters. This work enabled the authors to distinguish the properties of adsorption at different sites based upon different bond distances. From their work, it was concluded that at both sites, the bonding is dominated by ionic interaction supplemented with some covalent character due to donation from the adsorbed I anion to the Pt surface. This, the authors argue, causes the

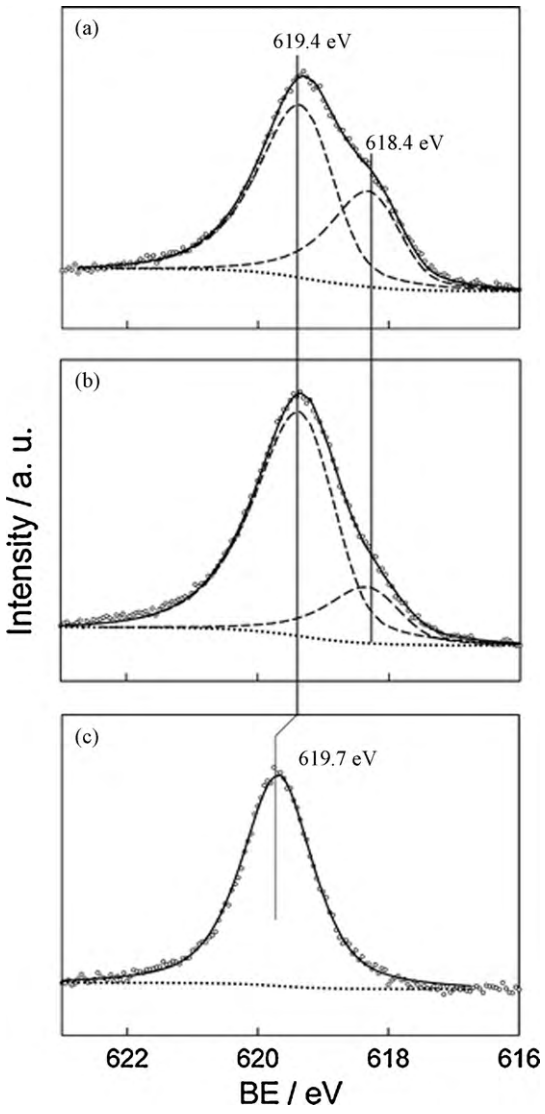


**Fig. 8.** Iodine 3d5/2 spectra for high coverage of iodine on (a) Pt(1 1 1), (b) Pt(1 1 1)/Ru with 0.5 monolayers of Ru, and (c) Ru(0 0 0 1). The spectrum in (a) can be fitted with two components (around 619 eV): the one at higher BE corresponds to iodine in threefold hollow sites and the other one corresponds to iodine on top sites. The spectrum in (b) can be fitted with three components: two at the same BE corresponding to iodine in hollow sites of Pt(1 1 1) and Ru(0 0 0 1) and one at higher BE for iodine on-top sites of Pt(1 1 1). The spectrum in (c) can be fitted with only one component. Ref. [26] (with permission).

I atom to be drawn closer to the Pt surface and at shorter distances has important consequences in changes in the work function and binding energy values. At closer distances, the BE value becomes larger.

### 3.4. Palladium particle size in formic acid electrooxidation

Formic acid electrooxidation has been studied on commercial, unsupported Pd nanoparticle catalysts of 9 (±2.5), 11 (±3), and 40 (±15) nm in size in a sulfuric acid electrolyte and analyzed by XPS [28]. Prior to experimental analysis, these nanoparticles were immobilized on a gold disk [24], were electrochemically reduced at 0.10 V, and further stabilized at 0.5 V (vs. RHE, all potentials are quoted with respect to RHE) for 20 min. This procedure produced a clean Pd surface where the Pd nanoparticles were thick enough to suppress the Au XPS peaks. XPS measurements revealed a relationship between particle size and electronic structure, showing no evidence towards formation of $PdH_x$ [94]. The most reactive catalyst for formic acid oxidation consisted of the smallest Pd nanoparticles. Such nanoparticles (9 and 11 nm) displayed the greatest current density (0.21 mA cm$^{-2}$ from 0.15 mA cm$^{-2}$) and Pd $3d_{5/2}$ BE shift (335.33 ± 0.03 and 335.25 ± 0.03 eV) and the greatest VB center downshift (2.64 ± 0.06 and 2.59 ± 0.06 eV) with respect to the Fermi level when compared to bulk Pd(1 1 1) (BE Pd $3d_{5/2}$ = 335.10 ± 0.03 eV and VB center = 2.49 ± 0.06 eV, respectively). That is, the d-band center was lowered in the smallest nanoparticles which showed the highest formic acid oxidation reactivity.

In developing a correlation for size and reactivity, only initial state effects were considered. This was done because the relaxation and screening of core holes (final state effect) are expected to converge at the bulk limit (particles with a diameter ca 10 nm and larger), based on earlier studies [10]. The initial state effects resulted in d-hybridization brought on by lattice strain since smaller particles have shorter bond distances. Hybridized d-bands are known to affect XPS BE's [10,21,35] since the d-orbitals form stronger bonds between metal atoms, reducing the potential of metal atoms to form strong bonds with adsorbed reactants. The lattice strain effect and its electronic consequences are the reasons for the enhanced reactivity of oxidizing formic acid. The electronic influences that result from lattice strain alter the BE's and the positions of the d-band. This was also noted in earlier electrochemical NMR experiments in which the Knight shift (the shift in the bulk local DOS) was observed for unsupported polycrystalline Pt [95], see also Refs [96,97]. From the reactions listed below, the rate of formic acid transformation to $CO_2$ (reaction 1) is the highest at the surface that is free of $(COOH)_{ads}$. The smallest Pd nanoparticles (particles with the lowest d-band center) bind the hypothetical $(COOH)_{ads}$ intermediate less strongly which reduces the $(COOH)_{ads}$ coverage (reactions 2 and 3) enhancing the rate of reaction 1.

$$HCOOH_{bulk} \rightarrow 2H^+ + 2e^- + CO_2 \quad (1)$$

$$HCOOH_{ads} \rightarrow (COOH)_{ads} + H^+ + e^- \quad (2)$$

$$(COOH)_{ads} \rightarrow CO_2 + H^+ + e^- \quad (3)$$

### 3.5. Chemical state of Ru submonolayers on a platinum electrode

Various bimetallic catalysts have been prepared in order to develop a catalyst superior to Pt. While not cost effective, Pt-Ru alloy has been shown to be a more efficient catalyst than pure Pt in DMFC anodes, and is therefore a widely studied system [98–101]. Ruthenium present on the platinum electrode surface has been shown to promote the methanol oxidation reaction [5]. Laboratory studies on model surfaces involve platinum electrodes containing controlled amounts of ruthenium deposited on the surface from the electrolyte [5] or via vacuum deposition [102]. Among low index Pt($h\,k\,l$) substrates containing ruthenium on the surface, the highest catalytic activity has been displayed by Pt(1 1 1)/Ru. Scanning tunneling microscopy (STM) has shown that ruthenium exists as a network of nanodispersed islands on platinum electrodes, and that methanol electrooxidation occurs at the edge of these ruthenium islands [103,104]. As we describe below, the XPS BE shifts and intensities have made it possible to identify the appropriate composition of Pt-Ru alloys to be effective catalysts.

Previously, knowledge about the chemical state of ruthenium during methanol electrooxidation was unclear. Ruthenium oxides were usually found as the main catalyst components [105,106] on Pt/Ru catalysts through XPS, with metallic ruthenium appearing on the electrodes after methanol electrooxidation was carried out for extended periods of time [105]. Kim et al. have shown by XPS that metallic Ru is necessary for effective electrooxidation of methanol in acidic media [107]. For this study, spontaneous depo-

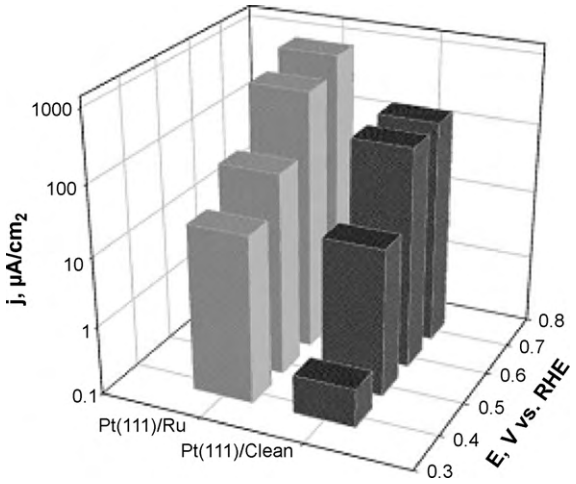


**Fig. 9.** Block diagrams of current density due to methanol oxidation under chronoamperometric conditions at different potentials for Pt(1 1 1)/Ru (after 2 min of deposition). Current density measured after 10 min of polarization in 0.1 M $HClO_4$ + 0.1 M methanol at 25 °C. The Ru enhancement was found to be ∞ at 0.30 V, 81 at 0.40 V, 5.9 at 0.50 V, 3.4 at 0.60 V, and 5.4 at 0.70 V. Ref. [107] (with permission).

sition was done in 0.5 mM $RuCl_3 \cdot xH_2O$ in 0.1 M $HClO_4$ for 2 min at open circuit (roughly 0.90 V vs. RHE). In concurrent experiments, constant potential electrolysis was performed at 0.30 V from a 2 M ruthenium nitrosylnitrate solution in 0.5 M $H_2SO_4$. Both procedures yielded 0.20 ML of ruthenium coverage. This is the optimum coverage found for Pt(1 1 1)/Ru surfaces [5,103]. Potentials are quoted with respect to the RHE.

Methanol electrooxidation data (Fig. 9) indicate that the Pt(1 1 1)/Ru surface is more active than Pt(1 1 1) in the potential range negative of a threshold value located at the beginning of the double layer range for the Pt electrode. The enhanced catalytic activity of Pt(1 1 1)/Ru compared to Pt(1 1 1) is especially apparent at potentials less than 0.4 V and becomes shallower at more positive potentials, i.e. the ruthenium activity enhancement factor is infinity at 0.3 V while at 0.4 V this value becomes 81, and further increases in potential significantly reduce this value. From XPS measurements in Fig. 10, an increased potential from 0.30 to 0.60 V lead to the formation of more Ru-oxides. From peak-fitting analyses, three spin-orbit $3d_{5/2}$ doublets were observed and assigned to $RuO_2$ (281.0 eV), $RuO_3$ (283.0 eV), and metallic Ru (280.3 eV) in the spectra. Fig. 10a shows the Ru 3d XPS for Ru deposited from nitrosylnitrate at a potential of 0.3 V. It is clear that Ru is predominantly metallic. For deposition at higher potentials (0.40–0.60 V, Fig. 10b–d), progressive oxidation of Ru occurred. The oxides formed upon exposure to higher potentials could be reduced back to metallic ruthenium when exposed to lower potentials. The decrease in potential (Fig. 9) involves an increase of $RuO_2$ and $RuO_3$. These Ru oxides acted as a catalytic de-enhancer rather than an enhancer for the electrooxidation of methanol. The quantitative correlation between the surface and reactivity data in Fig. 9 and Fig. 10 show the presence of metallic ruthenium in the full potential range causing this surface to be more active than Pt(1 1 1). After correlating ruthenium valence states to methanol oxidation reactivity, the authors concluded that the presence of a ruthenium metallic phase, possessing a weakly bound oxidation precursor, is a prerequisite for effective methanol oxidation electrocatalysis. This precursor is an activated water molecule supplying the oxygen necessary to transform surface CO to $CO_2$ at the edge of ruthenium islands on the platinum electrode [108]. These results coincide with those of Crown et al. [104] who reported that the gain in methanol electrooxidation activity correlates with an increase in metallic ruthenium on Pt/Ru nanoparticles.

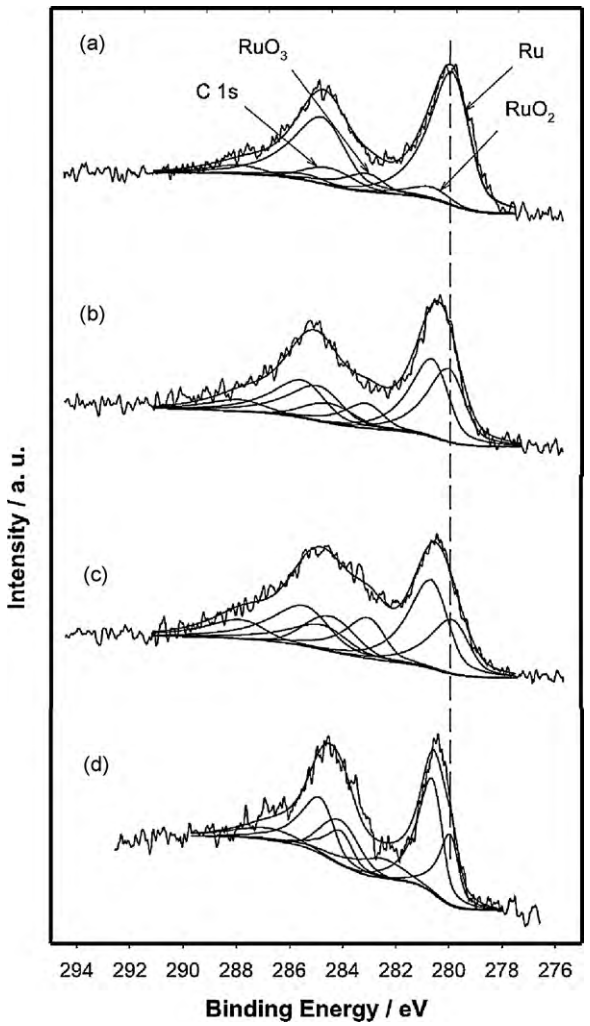


**Fig. 10.** XPS of Ru 3d region after deposition from 2 mM $Ru(NO)(NO_3)_3$ in 0.5 M $H_2SO_4$ at 0.30 V for 1 min. (b) As in (a), but following deposition at 0.30 V the electrode potential was stepped to 0.40 V for 1 min. (c) As in (a) following the deposition at 0.30 V the electrode potential was stepped to 0.50 V for 1 min. (d) As in (a) following the deposition of 0.30 V the electrode potential was stepped to 0.60 V for 1 min. (No further change was found in the range from 0.60 to 0.9 V.) The vertical line shows the metallic Ru signal. Ref. [107] (with permission).

### *3.6. Experiment and theory of methanol and formic acid decomposition on Pt-Ru nanoparticle catalysts*

We will show below how XPS, chronoamperometry (CA), and cyclic voltammetry (CV) data work in tandem to provide a more comprehensive understanding of the electrochemical behavior found at the surfaces of Pt-Ru bimetallic catalysts. CA experiments were performed to determine a correlation between the center of the d-band of these alloys and their rates of methanol and formic acid electrooxidation. Electrooxidation currents for methanol and formic acid were normalized to the catalysts' surface area to ensure that particle size does not influence the data.

As previously mentioned, it is widely regarded that the enhanced catalytic activity of bimetallic catalysts can be attributed to the bifunctional mechanism [109,110] as well as the electronic effect [9,11]. The bifunctional mechanism describes the enhanced catalytic properties of alloyed metals, where each metal plays a different role to have an overall synergistic effect on the reaction process. Despite the large amount of work [3,24,27,28,111–113] the relationship between surface electronic structure and catalytic activity towards electrooxidation of organic fuels is not completely

understood. Rigsby et al. studied the effects of electronic structure of Pt-Ru alloy on the reactivity of methanol and formic acid (through synchrotron XPS and electrochemistry) in order to understand the influence of the electronic effect on the catalyst [25]. Samples of Pt black, Pt90Ru10, Pt80Ru20, Pt67Ru33, Pt50Ru50, Pt40Ru60, Pt34Ru66, and Ru black were studied. Photon energies of 160, 370, and 650 eV were used and the standard error for the core-level BEs was 0.03 eV.

The Pt $4f_{7/2}$ binding energies were found to increase with increasing Ru content, which corresponds to a shift in the d-band center of Pt $4f_{7/2}$ towards a higher binding energy. The Pt $4f_{7/2}$ BE shift was greater than the Ru $3d_{5/2}$ BE shift, which has been observed in several cases [26,27]. Specifically, the Pt 4f BE shift decreased by ca. 0.5 eV when going from a small amount of Pt to pure Pt crystal, while the Ru 3d BE went from 280.00 eV with 10% Ru, in PtRu alloy, up to 280.14 eV for Ru black. These BE shifts cannot be explained by charge transfer since the donating and receiving levels for Pt and Ru are comparable in size (which would suggest similar core-level BE shifts). Bagus et al. demonstrated with *ab initio* studies, by varying the bond distances in models of pure and mixed particles, that the ΔBE shifts were the result of lattice strain [23]. Accordingly, the Ru 3d BE was less sensitive to changes in bonding distance than the Pt 4f BE. These differences arise as a result of the open 4d-shell of Ru, which contrasts to the almost filled d-shell of Pt. Addition of Ru caused the Pt lattice to undergo compressive strain, which shortened the Pt-Pt bonds. This shortened bond distance caused the d orbitals to overlap more and resulted in a downshift in the center of gravity of the d-band with respect to the Fermi level in order to maintain constant filling and to conserve energy.

The electrooxidation of methanol was investigated on a series of samples using CA at 450 mV vs. RHE. Methanol electrooxidation on Pt/Ru surfaces proceeds through a dual-pathway mechanism at positive potentials. These processes involve a strongly adsorbing CO intermediate [109,110,114] that poisons the Pt catalyst. The removal of CO is facilitated by surface oxygen species, which react to form $CO_2$. This is accomplished through Ru which is known to activate water to form the necessary surface oxygen species via the bifunctional mechanism [101,109,114]. Reactivity was shown to depend on the catalyst composition, as the current density was different for each sample at a given time. Further, the reactivity decreased until a steady-state was achieved. The authors surmised that this decreased reactivity was from CO poisoning the sites on the Pt catalyst [114,115]. The electronic effect had a minor role in the electrooxidation of methanol based on the volcano behavior of the steady-state current density as a function of Ru content (Fig. 11). As noted, increasing Ru content increases the core-level BE of Pt $4f_{7/2}$. An increase in the BE of Pt $4f_{7/2}$ would lead to a weaker adsorption of CO. Therefore, if the electronic effect was the key mechanism, the reactivity at high CO coverage should show a linear relationship with Ru content. Instead of the electronic effect, the volcano behavior demonstrated in this experiment showed that the bifunctional mechanism was the dominant contribution to methanol oxidation. This qualitatively verifies conclusions made by Lu et al., who found that the bifunctional mechanism contributed more significantly to reactivity than the electronic effect [116].

The volcano behavior produced by the bifunctional mechanism was most likely the result of ensemble effects. It is assumed that the active site consists of three Pt atoms and one Ru atom. Theoretical probability calculations for such an ensemble of atoms at the surface at room temperature have been performed by Gasteiger et al. [109,117]. They found that the probability distribution curve peaked at 10% atomic Ru. The maximum activity in this study was at a nominal composition of 20–30% Ru (Fig. 11), which was shown to have 17–18% atomic Ru at the surface based on X-ray powder diffraction (XRD) measurements. This disagreement between

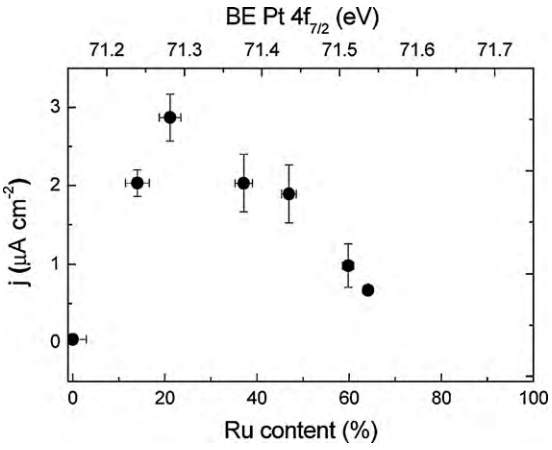


**Fig. 11.** Volcano plot of methanol electrooxidation on Pt/Ru nanoparticles. Uncertainties were calculated from at least three independent measurements. The current density is found to peak at a nominal composition of about 20–30% Ru. This behavior cannot be explained by the electronic effect alone. Rather, it proves that the bifunctional mechanism is dominant. For PtRu catalysts, an increase in the Pt $4f_{7/2}$ binding energy would lead to weaker adsorption of the poisoning CO species, which would lead to a decrease in the poisoning effects. If the electronic effect was the dominant enhancement mechanism, the reactivity at high CO coverage should also increase with increasing Ru content, in contrast to what is observed. Ref. [25] (with permission).

the experimental results and the calculated probability suggests that there are more contributions to the enhanced catalytic activity of the Pt-Ru alloy than just from the bifunctional mechanism. The data could not be separated to determine the extent of the various mechanisms, but is in agreement with previous results [109,114,116,118]. These experiments demonstrated that several factors enhancing the electrooxidation of methanol work simultaneously and that separating these effects to determine their relative contributions and importance can be difficult, if not impossible.

Since the results of methanol electrooxidation were inconclusive in determining the measure of the electronic effect, it was decided to investigate the electrooxidation of formic acid. Formic acid is a promising fuel for study based on its ease of electrooxidation [119–126]. The chemical is known to go through three reaction pathways [96,97]: a direct pathway to $CO_2$, an indirect pathway through a CO intermediate, and an adsorbed formate pathway. Previous studies have shown that at low potentials (below ca. 0.6 V vs. RHE), and at short reaction times, the direct HCOOH oxidation pathway is predominant on Pt electrodes, making the amount of adsorbed intermediates negligible [97,111]. This observation provides an opportunity to study the electronic effects separate from the bifunctional mechanism since there is no CO intermediate in the direct pathway.

The current densities were collected for the Pt-Ru alloys at 500 mV vs. RHE over a period of 1 h. Based on the known reaction pathways, the main poisoning species was presumed to be CO [96,97,111,127,128]. At steady-state, a volcano behavior was observed when current density was plotted against catalyst composition. However, at short (3 s) reaction times, a linear correlation was observed, where the instantaneous current density decreased with increasing Ru content. The turn over frequency (TOF) for each Pt active site was calculated to verify a correlation between current density and Ru content. This value normalizes the current with respect to the number of available Pt sites. Formic acid decomposes on Pt via a dehydration reaction that produces surface CO, which is oxidatively removed at potentials above ~0.4 V vs. RHE [111]. This molecule also decomposes on Ru surfaces [101,109,114]; however, from the current at 0% compared to 100% Ru, the current on Pt is much greater than that on Ru. So while there is some contribution from electrooxidation on Ru, this value is very small. The TOF at

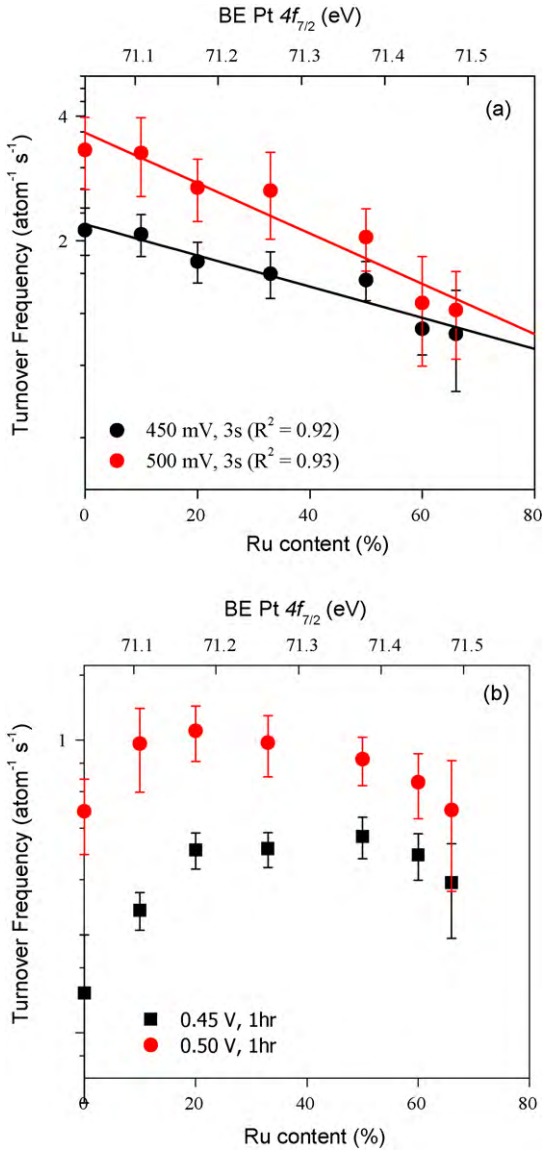


**Fig. 12.** Turnover frequency of Pt sites as a function of the Ru amount and the Pt $4f_{7/2}$ binding energy at (a) 3 s and (b) 1 h. Measurements were done in 0.2 M HCOOH + 0.5 M $H_2SO_4$ and recorded at 450 and 500 mV vs. RHE. In (a) the TOF at short reaction times is found to decrease linearly as a function of both increasing Ru content and increasing Pt $4f_{7/2}$ binding energy, while in (b) the TOF at steady-state (1 h) shows a volcano dependence on the Ru amount and Pt $4f_{7/2}$ binding energy. Ref. [25] (with permission).

short reaction times (3 s), where the amount of adsorbed species poisoning the surface was assumed to be negligible, was found to decrease linearly versus increasing Ru content and increasing Pt $4f_{7/2}$ BE (Fig. 12a). These results demonstrated the role of catalyst electronic structure in the electrooxidation of formic acid at this alloy, following the prediction of Nørkov's d-band center theory. The TOF at steady-state (1 h) showed a volcano dependence on the Pt $4f_{7/2}$ BE and Ru amount (Fig. 12b).

### 3.7. *Electronic structure of palladium thin films deposited on metallic surfaces*

The presence of an adsorbate may change the XPS core-level BE's of the surface atoms to which the adsorbate is bound. Thus for CO/Pd(1 1 0), the presence of the CO shifts the 3d BE of the Pd atom to which the CO is bound to a higher BE by over 1 eV [129]. Furthermore, the BE of an adsorbate metal atom on a metal surface may be shifted from the BE of a surface atom of a crystal of the pure adsorbate [130]. This latter shift is called an adsorbate (or adlayer) core-level shift (ACLS) where the ACLS is rigorously defined as the difference between the BE of a core-level of an adlayer of metal A on a metal crystal B and the BE of a surface atom of the pure metal A. The ACLS can provide critical information about the electronic character of metal adlayers and, hence, ACLS's are relevant for the study of bimetallic catalysts. Early work of Rodriguez, Campbell, and Goodman involved studies of CO adsorbed on Pd adlayers on Re(0 0 0 1) where the CO adsorption strength to the Pd adlayer and the Pd ACLS's were correlated [11,131]. Rodriguez et al. proposed that initial state charge transfer between the Pd overlayer and the Re(0 0 0 1) substrate was responsible for the Pd ACLS. However, later theoretical models were proposed to explain the chemical behavior of Pd/Re(0 0 0 1) and other bimetallic systems [132]. Further theoretical studies from Pallassana et al. [133], built upon the work of Nørskov and Hammer [6], correlated the surface electronic properties of Pd/Re(0 0 0 1) to the chemisorption bond of hydrogen on this surface. It was found that the d band center for Pd atoms on Re substrate shifted 0.72 eV below the BE value for bulk Pd, with a corresponding reduction in the chemisorption bond energy of 0.4 eV. In order to verify these later theoretical studies, Mun and co-workers analyzed the electronic structures of Pd thin films grown epitaxially on Re(0 0 0 1) with high-resolution, synchrotron-based photoelectron spectroscopy [134]. A clean Re(0 0 0 1) surface was obtained through argon-ion sputtering and annealing at 1500 K. The Pd monolayer was deposited by e-beam evaporation. During deposition, the temperature was 300 K, with the deposition rate of Pd set to one ML every 7 min. Surface alloy formation was avoided by not annealing after deposition. The pressure during deposition and XPS measurements was ca $5 \times 10^{-10}$ Torr.

Initially, two different Pd states on the surface of Re(0 0 0 1) appeared with population varying with coverage. The higher binding energy state was present exclusively at coverages up to 1 ML. This peak remained at 335.7 eV and can be assigned to the BE of Pd atoms at the Pd/Re(0 0 0 1) interface. From 1.5 to 2.5 ML, a new peak appeared at a lower BE of 335.0 eV, inferred to be from Pd atoms in the multilayer (possibly from Pd(1 1 1) oriented islands) [135]. At 5 ML this peak dominated the intensity of the $3d_{5/2}$ spectra. The ACLS for the Pd monolayer was determined to be +1.0 eV, a value slightly higher than the ACLS of Pd thin film on Re determined by Goodman and Rodriguez (+0.7 eV) [11,131]. This greater shift might be due to the higher resolution of the instrument. The Re $4f_{7/2}$ signal was acquired simultaneously with the Pd $3d_{5/2}$ and remained constant to within 0.1 eV. This observation is consistent with Goodman and Rodriguez's previous observations [11,131]. The manner in which these two Pd $3d_{5/2}$ formed implies an island growth mode.

Ultraviolet photoemission spectroscopy valence-band spectra for Pd thin films on Re(0 0 0 1) is given in Fig. 13. To better identify the peaks of the 2D Pd layer at the interface with Re(0 0 0 1), a scaled valence-band spectrum of clean Re(0 0 0 1) was subtracted from each spectrum and re-plotted. As Pd coverage neared 1.0 ML, a reduction in the DOS at the Fermi level was observed along with new features shown as A, B, and C. Along with these peaks, there is enhancement of broad features (D and E) that appeared to maximize at 1.0 ML. When the Pd coverage increased to 2–3 ML, the features labeled B1 and B2 began to emerge and the total DOS resembled Pd(1 1 1) [136]. The states that are closest to the Fermi level, A-C, were observed upon Pd deposition and are characteristic of isolated Pd atoms, dimers, and trimers on Re(0 0 0 1). The broad features at D (BE = 3.8 eV) and E (BE = 4.5 eV) show around 0.8 ML coverage and become most resolved between 1.0 and 1.2 ML of Pd coverage. Peaks C–E correspond to states that are most characteristic of the 2D Pd layer at the interface. Spectra at 1.5 ML and further MLs show strong features of new states. These states are characteristic of bulk Pd(1 1 1).

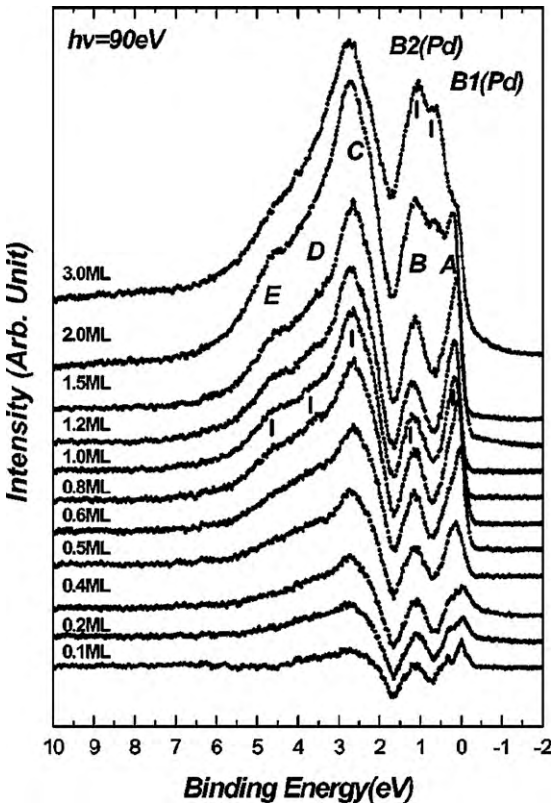


**Fig. 13.** Valence-band difference spectrum of Pd on Re(0 0 0 1) obtained by subtraction of a scaled spectrum from clean Re(0 0 0 1) substrate at 90 eV. This difference spectra was performed in order to identify more clearly the partial DOS of the 2D Pd layer at the interface with Re(0 0 0 1). Ref. [134] (with permission).

In order to experimentally verify the d-band center metric suggested by Nørskov, the experimental values for the d bands at 1 ML Pd/Re(0 0 0 1) and 3.0 ML Pd/Re(0 0 0 1) collected at 90 eV were used from Fig. 13 along with employing the mathematical definition used by Hammer and Nørskov [137]. These values were 2.80 (1 ML) and 2.46 eV (3 ML) with a d-band shift of −0.34 eV. Compared to gradient-corrected DFT periodic slab calculations where the band structure is at 2.70 eV (1 ML) and 2.39 eV (3 ML) with a d-band shift of −0.31 eV [133]. There is excellent agreement between the experimental values and the calculated band structures, especially in the shift of the d-band center from the Fermi level for the 2D Pd layer at the interface relative to the Pd multilayer. In conclusion, there was a shift to a higher BE for both Pd $3d_{5/2}$ core-level and Pd valence band peaks for a Pd ML at the Re(0 0 0 1) interfaces versus a Pd(1 1 1) surface layer. A core-level chemical shift in this instance would be interpreted as a result of charge transfer between the adlayer and the substrate atoms, in this case it would be from Pd to Re [11,131]. The shift in the valence band DOS away from the Fermi level would be interpreted as a band-filling charge transfer, such as donation of d electron charge by Re to Pd. Interaction between Pd and Re atoms at the interface results in charge accumulation in the interfacial region on top of Re atoms and charge depletion from both Pd and Re atoms. This causes the Pd core-level to shift to higher binding energy. The center of the Pd electrons shifts downward towards the substrate, forming a potential barrier in the interfacial region that lowers the energy of the d valence electrons. This causes the d band center to shift away from the Fermi level. Pallassana et al. showed that the d electron count in the Pd interfacial layer was the same as that in a Pd(1 1 1) surface layer [133]. From this, there is no band filling by electron donation from the substrate. The correct physical picture for the electronic modification is explained by substrate-induced charge polarization in the Pd layer.

### 3.8. Irreversibly adsorbed arsenic on Pt(1 1 1)

Kolb's group has explored the chemical composition of an irreversibly adsorbed arsenic layer on Pt(1 1 1) in sulfuric acid solution through XPS [138]. This work highlights the power of XPS for obtaining chemical information on adlayers. Earlier work has shown that submonolayers of As undergo a redox transformation at the surface without desorption of the As surface adspecies. This earlier work utilized cyclic voltammetry to study the irreversible deposition of As on Pt(1 1 1) and Pt(1 0 0) [139–141]. From these previous studies, a surface redox reaction has been proposed with a valence state change from As(0) to As(III) [140] or As(II) [141]. The irreversible adsorption of As on Pt electrodes remains poorly understood, as there is some uncertainty about the nature of the surface redox system. An XPS system with an electrochemical cell attached to the main UHV chamber was employed to determine the valence state change for the adsorbed As layer on Pt. Deposition experiments were performed utilizing two different methods: the first method involved immersing the bare Pt(1 1 1) crystal into a 0.1 M $H_2SO_4$ + 3.5 mM As(III) solution at +0.5 V, then scanning in the negative direction to +0.25 V (vs. Ag/AgCl) whereupon the electrode was emersed after a scan in the positive direction to various values; the other method involved crystal immersion into a 0.1 M $H_2SO_4$ + 3.5 mM As(III) solution at a given potential for 180 s to ensure saturation coverage, and subsequent emersion at this potential. The valence states of As and their change with potential were observed based on chemical shifts for the As 3d level. Peaks in the XPS spectra around 41 eV could be assigned to As(0) [142,143], while those around 44 eV were assigned to As(III), given that different As(III) species appear between 43.4 and 45.0 eV [142–145]. The total amount of As on the electrode surface was in good agreement with the corresponding charge-derived coverage obtained through CV. The first method observed surface coverages up to 0.41 ML (when emersed at +0.25 V), while the second technique observed coverages around 0.25 ML. The authors found that the amount of As(0) and As(III) on the surface, as measured through XPS, indicated some change in surface composition during or after electrode emersion, while the cyclic voltammograms suggested a complete valence state change with potential. That is, all As adatoms are in the zero-valent or three-valent state at potentials negative or positive to the surface redox feature around +0.33 V in the CV. It was suggested that partial double layer collapse caused about 20–30% of the total amount of As to undergo a redox reaction in the emersed state. This leaves around 0.06 ML of As(III) at negative potentials (at which only As(0) is present *in situ*) and roughly a similar amount of As(0) at positive potentials (at which only As (III) is expected to be on the surface). These problems have also been encountered with Te/Pt(1 1 1) systems, and show that an experimentalist should be cautious when performing quantitative analysis with an *ex situ* technique. Another problem from this study, related to the low energy resolution of the equipment (the overall resolution was reported to be 0.8 eV), was the lack of specifying the various oxygen-containing species. The chemical shifts in the O1s region of the XPS spectrum were too small for accurate assignment. This problem, however, is potentially remedied with the use of a synchrotron source, as described below.

## 4. Applications of XPS in studies of direct relevance to fuel cell electrocatalysis

### 4.1. Outline

Below, we discuss applications of XPS that are of direct relevance to fuel cell electrocatalysis. This section will begin with an

early experiment involving XPS performed on platinized carbon electrodes followed by information obtained through XPS on several anode and cathode electrocatalysts that provides insight into developing more powerful electrocatalysts for fuel cells.

### 4.2. Pioneering investigations by Goodenough and Hamnett

Goodenough and Hamnett analyzed platinized carbon with respect to oxidation of methanol in the direct methanol fuel cell (DMFC) [146]. (Platinized carbon, or Pt-carbon electrodes are known to have enhanced oxidative catalytic activity over bulk Pt that cannot be ascribed to simple surface-area effects.) XPS was used to study the oxygen species present in the Pt-carbon in relation to the oxidation process. Before methanol oxidation three Pt species were present. The Pt with the lowest BE was assumed to be metallic Pt (with $4f_{7/2}$ = 71.2 eV and $4f_{5/2}$ = 74.8 eV). The two other species are oxidized Pt: a doublet for $Pt4f_{7/2}$ at 73.8 eV and $4f_{5/2}$ at 77.2 eV roughly indicate Pt(II), and the other doublet for $4f_{7/2}$ at 74.9 eV and $4f_{5/2}$ at 77.9 eV suggests Pt(IV) [147–151]. Not only can the data display the different oxidation states, they also suggest that the spin-orbit splitting depends on the oxidation state of the metal and hence may provide an additional fingerprint for identification purposes. After anodic polarization, the amount of the oxidized Pt increased to yield only the BEs of the fully oxidized Pt. The lower overpotential for methanol oxidation on the platinized carbon (vs. that of Pt black) was attributed to the formation of active surface oxygen on Pt particles (from water molecules) at sites around the methanol oxidation intermediate. These active oxygen sites were proposed to be the B5 sites, where an adatom of the active oxygen species was coordinated to five surface Pt atoms. These sites are formed on surface steps, where there is no competition for chemisorbed methanol molecules. This so-called B5 site is an electron poor region at the Pt-carbon interface, making it highly susceptible to water attack [152]. The susceptibility of these electron poor sites to water attack would be enhanced through Pt electron donation to the substrate. There was an observed +0.3 eV shift in the Pt 4f regions of the XPS spectra for the supported Pt electrodes, confirming electron transfer to the substrate. Even with the enhanced activity over bulk Pt, the activity of the Pt-carbon slowly decreased after approximately a 20 h polarization experiment. A build up of an excess oxygen species on the Pt was responsible for the decreased activity and could be reduced by returning the electrode to open circuit in the methanol-containing media (ca. 0.2 V vs. NHE). Goodenough and Hamnett concluded that the enhanced methanol oxidation activity of the Pt-carbon was due to presence of active oxygen on the electrode and not the weaker interaction of methanol with Pt. The increase in oxidized Pt at the surface, formed on methanol adsorption sites, could be attributed to the decrease in activity.

### 4.3. Chemical and electronic effects of Ni, PtNi and PtRuNi alloy nanoparticles towards methanol electrooxidation

Park et al. investigated Pt, Pt/Ni, Pt/Ru/Ni, and Pt/Ru alloy nanoparticle catalysts in relation to methanol oxidation processes in the DMFC [153]. As previously mentioned, Pt/Ru catalysts are known to show better catalytic activity when compared to Pt alone in the presence of CO (Fig. 9). This is the result of the Ru-O bonding energy being similar to Pt-C bonding energy [154]. As such, Ru-O can easily oxidize the CO intermediate present on Pt to produce $CO_2$ (the bifunctional mechanism). For further discussion on Pt/Ru catalysts, please see Sections 3.5 and 3.6 as well as Refs. [98–100,155]. For Pt/Ni catalysts the energy of the Ni-O bond is ca 200 kJ/mol lower than that of Pt-C. As such, essential characteristics of Pt/Ni cannot be explained by the bifunctional mechanism. To obtain insight into DMFC electrooxidation mechanisms on Pt/Ni and Pt/Ru/Ni, XRD, XPS, transmission electron microscopy (TEM), and electrochemical measurements were performed.

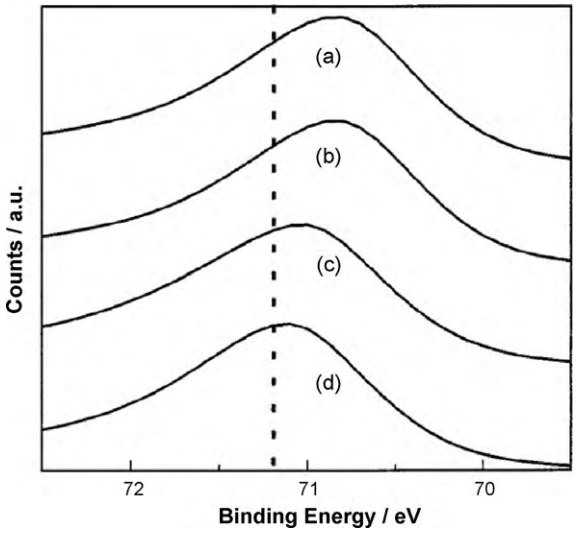


**Fig. 14.** Pt4f peak shift of Pt-based nanoparticles; (a)Pt/Ni(1:1), (b)Pt/Ni (3:1), (c) Pt/Ru/Ni (5:4:1), and (d) Pt/Ru (1:1). The dotted line is the Pt $4f_{7/2}$ peak position for pure Pt. The peaks are shifted from 0.17 for Pt/Ru/Ni (5:4:1) to 0.35 and 0.36 eV at Pt/Ni; that is, they are moving toward the lower Pt 4f biding energy. Because there is more metallic nickel in Pt/Ni(1:1)than in other Ni-containing formulations studied in this project, this data demonstrate that the spectral shift increases, at least semiquantitatively, with the amount of Ni metal present in the sample. Ref. [153] (with permission).

The nanoparticle catalysts were synthesized at room temperature with $MCl_x$ salts (where M = Pt, Ru, and Ni) using $NaBH_4$ as the reducing agent [156]. The nominal compositions for the catalysts were Pt/Ni (1:1 and 3:1), Pt/Ru/Ni (5:4:1 and 6:3.5:0.5), and Pt/Ru(1:1). TEM measurements showed that these nanoparticles were less than 4 nm in size. XRD showed alloy formation for all Pt/Ni, Pt/Ru/Ni, and Pt/Ru nanoparticles. The Pt/Ni and Pt/Ru/Ni alloy showed excellent catalytic activities compared to those of pure Pt and Pt/Ru. The onset potential for methanol oxidation was Pt/Ru/Ni (5:4:1, 0.261 V) < Pt/Ru (1:1, 0.265 V) < Pt/Ni (1:1) ~ PtRuNi (6:3.5:0.5, ca. 0.288 V) < Pt/Ni(3:1, 0.320 V) < pure Pt (0.350 V vs. NHE). XPS confirmed that chemical states of Pt were exclusively metallic. From the escape depth of about 2–3 nm for Pt, Ru, and Ni, it is evident that the entire bulk was the subject to XPS analysis. No XPS peaks for chloride were found, demonstrating that the metal salts were completely removed during washing. The major Ni component in each alloy was $Ni(OH)_2$. For Pt/Ni (1:1), the Ni in the sample consisted of metallic Ni (11.8%, BE 852.7), NiO (15.9%, BE 853.8), $NiOH_2$ (45.2%, BE 855.6), and NiOOH (27.1%, BE 857.3 eV). At Pt/Ni (3:1), the nanoparticle had metallic Ni (33.7%), and a decreased amount of Ni oxides. For Pt/Ru/Ni (5:4:1), the composition was 14.4% metallic Ni and 11.2% NiO. The ratio of the oxides in this sample was similar. Whether metallic Ni exists at or below the surface is unclear from this XPS investigation, based on the depth to which the utilized radiation penetrates the sample. Metallic Ru, $RuO_2$, and $RuO_3$ were detected on the Pt/Ru/Ni alloy as well.

The authors found that the Pt 4f binding energies for the Pt/Ni and Pt/Ru/Ni alloy nanoparticles were lower than those for clean Pt nanoparticles (Fig. 14). The peaks moved towards a lower Pt 4f BE from −0.17 eV for Pt/Ru/Ni (5:4:1) to −0.35 and −0.36 eV at Pt/Ni. These shifts were interpreted to result from modification of the Pt electronic structure by electron transfer from Ni to Pt. This is valid considering electronegativities of the three components: Pt, Ru, and Ni. In summary, the oxides that serve as the oxygen donors for the oxidation process, and the change in the electronic

structure of the Pt component in the alloys versus those in Pt and Pt/Ru collectively account for the enhanced methanol oxidation rates.

### 4.4. Palladium as methanol-tolerant cathode catalysts

Lee et al. studied Pd-based alloys, including Pd-Co, Pd-Ni and Pd-Cr alloys as methanol resistant electrocatalysts for the oxygen reduction reaction (ORR) in DMFCs [157]. The superior activity of Pd-based catalysts in comparison to pure Pd was found; the maximum activity of the catalysts was observed with samples containing ca. 60% Pd in the alloy compositions. Selectivity of Pd-based alloys towards ORR in the presence of methanol compared to Pt was observed, while Pd-Ni showed the highest activity in the presence of methanol. XPS analysis of the binding energy of Pd $3d_{5/2}$ peaks of the alloys (335.7, 335.5, and 335.6 eV for Pd–Co, –Ni, and –Cr, respectively) showed chemical shifts toward higher values compared to the value for Pd (335.2 eV). Since the shifted BE's are short of the BE for PdO (336.3 eV), the authors suggested the interaction between Pd and the second metal as the origin of the shifts. The XPS valence band spectra showed the value of the center of the d-band of Pd (1.5 eV) and Pd alloys (2.3, 1.9, and 2.7 eV for Pd–Co, –Ni, and –Cr), which are shifted to higher values because of the d–d band hybridization between Pd and the second metal. As electrons transfer from Co, Ni and Cr to Pd, to fill the d-band of Pd, the density of state (DOS) at the Fermi level decreases. The bond strengths of O and OH species on the surface are affected by the DOS at the Fermi level and filling of the Pd d-band by the electrons of the second element can weaken the chemisorption of O and OH adspecies on the Pd sites. The authors suggest that preventing the formation of Pd oxides on the surface contributes to the observed enhanced catalytic activity of Pd-based alloys.

### 4.5. Mixed-reactant fuel cells and methanol-tolerant cathodes

Mixed-reactant fuel cells (MRFC) use a mixture of fuel and oxidant, and – in concept – the separation of fuel oxidation and oxidant reduction is left to the selectivity of the electrocatalysts. MRFCs use different fuels, e.g., methanol, formic acid and ethanol, however reformed methanol and direct methanol MRFCs are the most popular [158]. The challenge of fuel cross-over in DMFCs and the need for methanol tolerant cathodes has encouraged the development of selective electrocatalysts which can be used in MRFCs.

Nitrogen-containing carbon nanostructures ($CN_x$) have been prepared from the decomposition of acetonitrile at 900 °C over silica and magnesia supports impregnated with Fe, Co, or Ni to test for methanol-tolerant cathodes in DMFCs and MRDMFCs [159]. The $CN_x$ fibers grown from supported Fe possessed the highest activity for ORR while Ni-containing catalyst showed the least activity. None of the $CN_x$ fibers showed activity for methanol oxidation. Despite the high activity of iron-containing catalysts, metal-free catalysts also demonstrated catalytic activity, which suggests that Fe centers are not the active sites but play a role in promoting the growth of nanofiber structures. A correlation between the fiber nanostructure acquired from TEM imaging and the activity of the catalysts was observed, and the abundance of stacked cup structure (more edge plane exposure) favors ORR activity. XPS characterization and analysis of N1 s spectra was used to determine the amount and identity of nitrogen groups in the catalysts, which revealed a correlation between the amount of N-pyridinic and the catalytic activity toward ORR. Since the N-pyridinic species are present on the edge plane structure, this observation correlates with the observed nanostructural relationship, however no definitive conclusion about the nature of the active sites was proposed [159,160].

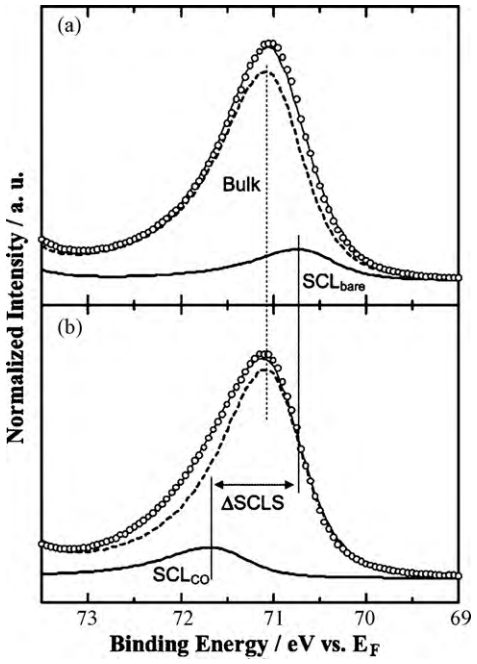


**Fig. 15.** Decomposition of Pt $4f_{7/2}$ spectra (open circles) for pure Pt electrode (a) before and (b) after the CO adsorption. Solid and dashed lines show the contributions due to surface and bulk core levels, respectively. The decomposition for (a) was carried out with the following assumptions: (i) The surface core-level (SCL) contribution was ca. 13% of the total intensity, estimated from the inelastic mean free path (IMFP, 1.9 nm) of Pt4f photoelectron excited with Al Kα. (ii) The bulk CL and SCL had the same characteristic parameters except for the BE and peak height. In (b) CO attenuated the bulk and surface peaks to the same degree. Consequently, peak fitting for (b) followed the same parameters as in (a). Ref. [80] (with permission).

### 4.6. Electronic structures of Pt-alloys for CO-tolerant anode catalysts

The electronic structures of Pt, $Pt_{58}Co_{42}$, and $Pt_{60}Ru_{40}$ have been investigated by the Watanabe group with respect to the hydrogen oxidation reaction (HOR) [80]. The experiments discussed here and in the next section involve an electrochemical-XPS (EC-XPS) set up discussed in the instrumental portion of this review. The magnitude of the Pt 4f surface BE shift for the Pt-Ru alloy was +0.39 eV and +0.19 eV for the Pt-Co alloy. A positive BE shift for an atom, in this case Pt, is associated with the loss of an electron from that atom. Based upon the work function values of Pt, Ru, and Co, an electron is transferred from Ru or Co to Pt. The positive shift in the $Pt4f_{7/2}$ peak is better explained by the difference between the work functions of Pt and the alloyed Pt. This results from rehybridization of the d-band along with the sp-band [161]. The work function change leads to a change of the catalyst Fermi level. An upshift in the reference level causes a downshift in the $Pt4f_{7/2}$ peak and the d-band center. After electrochemical stabilization in 0.1 M $HClO_4$, the $Pt_{58}Co_{42}$ electrode formed a skin layer. This outer layer of Pt, that is, the skin layer, protects the underlying bulk alloy against further dissolution [162]. The $Pt_{60}Ru_{40}$ electrode maintained its initial composition through the electrochemical stabilization in 0.05 M sulfuric acid. The core-level shift for $Pt4f_{7/2}$ for $Pt_{58}Co_{42}$ and $Pt_{60}Ru_{40}$ was 0.15 and 0.39 eV, respectively.

After the electrochemical stabilization and XPS measurements of the clean materials, CO adsorption experiments were performed. CO was adsorbed using CO-saturated solutions in the electrochemical cell chamber at 75 mV (vs. RHE). The XPS spectrum for Pt consists of contributions from surface and bulk Pt atoms, as shown in Fig. 15a [163,164]. The Pt 4f BE for surface core-level (SCL) is lower than the bulk, which is due to surface Pt atoms possessing narrower d-bands as a result of having fewer neighbors [108,166,167].

The CO adsorption shifted surface platinum XPS peaks to higher BE and also increased the FWHM, as shown in Fig. 15b. Previous reports have indicated that the SCL peak of Pt shifts to a higher BE once CO is adsorbed, while the bulk core-level peak is unperturbed [163–165]. The SCL shift for CO adsorbed on surface Pt atoms is a result of the Pt electron density being donated to CO [164,165]. The SCL shift values are 0.95 (Pt), 0.75 (Pt-Co), and 0.57 eV (Pt-Ru). From the $Z+1$ approximation and from the Born-Haber cycle, CO adsorption energies for each electrocatalyst were determined based upon SCL shift measurements and also via incorporating the CO adsorption energy of Au [165,168]. The CO adsorption energies were calculated to be 1.44 eV (Pt), 1.24 eV (Pt-Co), and 1.06 eV (Pt-Ru). This corresponds to a linear relationship between BE shifts and CO adsorption energies, where the Pt-CO bond becomes weaker in the order: Pt, Pt-Co, Pt-Ru. From this study, catalysts obtained from non-noble transition metals alloyed with Pt exhibited excellent CO-tolerant HOR activities. This high CO tolerance during HOR is the result of a weaker CO bond strength from modification of the electronic structure of Pt.

### 4.7. $O_2$ coverage at Pt-Fe alloy cathode for enhanced oxygen reduction reaction

Active cathode catalysts for the oxygen reduction reaction (ORR) are important in order to obtain highly efficient fuel cells. Preferably, the catalysts should contain minimized amounts of platinum because of both costs and availability. Several groups reported an enhanced ORR activity upon alloying Pt with Co, Fe, Ni, and other transition metals [3,169–171]. Surfaces of these alloys were found to have non-noble metal components removed, and the Pt surfaces rearranged. This outer layer of Pt, the skin layer (see above), protects the underlying bulk alloy against further dissolution [162], and shows enhanced ORR catalytic activity.

Watanabe et al. examined the amount of oxygen species on the Pt-skin layer surface of Pt-Fe alloy and compared them to pure Pt [172]. Utilizing EC-XPS, a Pt skin layer was produced on $Pt_{63}Fe_{37}$ by voltammetry in deaerated 0.1 M HF solutions, where three different types of oxygen species were identified at BEs of 529.6 eV, 530.5 eV, and 531.1 eV and 532.4 eV. The first two were assigned to oxygen ($O_{ad}$) and hydroxyl ($OH_{ad}$), while the other two were assigned to adsorbed water ($H_2O_{ad}$). The Pt skin layer from the Pt-Fe alloy had a higher affinity for $O_{ad}$ but less affinity for $H_2O$ when compared to a pure Pt electrode. The higher $O_{ad}$ coverage was attributed to the more active ORR observed on the Pt skin-type electrodes versus pure Pt. In deaerated solutions, the coverage of $H_2O_{ad}$ was much lower on the Pt skin layer, suggesting an adsorption preference for $O_2$. It was concluded that the increased preference for $O_2$ was not obstructed by $H_2O_{ad}$, and that the modified electronic properties of the surface Pt skin layer came from the underlying Pt-Fe alloy.

These researchers also investigated oxygen species from adsorbed water on Pt(1 1 1) and compared the results to polycrystalline Pt [173]. Four oxygen species were identified with nearly the same BEs as above (from XPS). The first two, at 529.6 eV and 530.5 eV, were assigned to $O_{ad}$ and $OH_{ad}$, while the other two, at 531.1 eV and 532.6 eV, to two types of adsorbed water molecules, ($H_2O_{ad,1}$ and $H_2O_{ad,2}$). As discussed above, water molecules form an ice-like bi-layer [82]. Therefore, the species at 531.1 eV could be assigned to the first layer of water molecules, which directly binds to the surface of Pt, whereas the peak at 532.6 eV could be assigned to the second layer of water. Fig. 16 compares the properties of Pt(1 1 1) to polycrystalline Pt. Coverages for the different oxygen species were calculated from deconvoluted O1 s peak intensities normalized with respect to Pt 4f. The $OH_{ad}$ appeared on Pt(1 1 1) at $E > 0.60$ V following the anodic current in the "butterfly" region [174,175]. The coverage by $OH_{ad}$ and $H_2O_{ad,1}$ was found to be almost equal to each other at $E = 0.80$ V, reaching a maximum at 0.68 V (vs. RHE). This is in a good agreement with the previously reported bilayer coverage [82,84]. A model was proposed, which depicted the most stable structure among the mixed $OH_{ad}$ and $H_2O_{ad,1}$ forms based upon a mixed hydrogen bonding network [176]. The decrease in $H_2O_{ad,1}$ at $E > 0.80$ V suggests the network became weakened and $H_2O_{ad,1}$ became unstable on the surface. At $E = 0.90$ V, the oxygen coverage began to increase while that of $OH_{ad}$ decreased, suggesting that $O_{ad}$ originated from $OH_{ad}$. At $E > 1.00$ V, $OH_{ad}$ and $O_{ad}$ increased. This increase was observed on polycrystalline Pt at 0.80 V. The formation of $O_{ad}$ on Pt(1 1 1) appears nearly at the same potential as on polycrystalline Pt; however, $OH_{ad}$ forms at a much lower potential than for polycrystalline Pt. This implies that $OH_{ad}$ formation is sensitive to a crystal face structure, whereas the formation of $O_{ad}$ is less dependent on the structure. In short, the oxygen species for the two electrodes varies with respect to the applied potential as well as with the crystal faces.

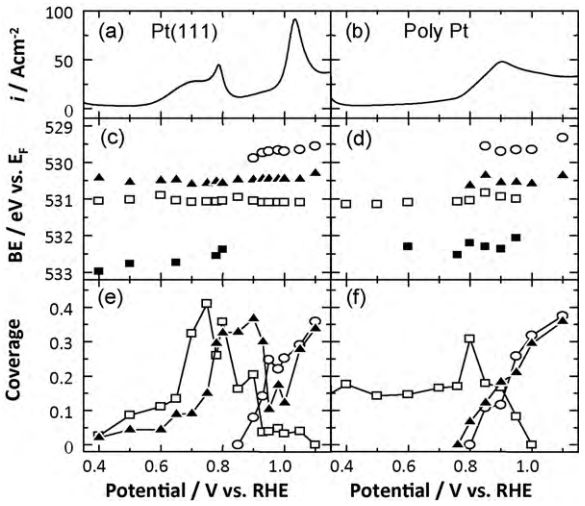


**Fig. 16.** Comparisons of the properties at Pt(1 1 1) single-crystal and poly-Pt electrodes in 0.1 M HF solution purged with $N_2$: voltammograms (50 mV $s^{-1}$) at (a) Pt(1 1 1) and (b) poly-Pt. Deconvoluted BEs for different oxygen species at (c) Pt(1 1 1) and (d) poly-Pt,with the coverage changes of each oxygen species as a function of electrode potential at (e) Pt(1 1 1) and (f) poly-Pt. Symbols: (○) $O_{ad}$, (▲) $OH_{ad}$, (□) $H_2O_{ad,1}$, and (■)$H_2O_{ad,2}$. Ref. [173] (with permission).

These studies have given better insights into the ORR mechanism at the Pt skin layer through the quantitative correlation between catalytic activity and the species present on the electrode surface. This also provides clues to designing high-activity electrocatalysts.

### 4.8. Modifying activity of an electrocatalyst for ORR by tuning the surface electronic structure

Tuning the surface electrocatalytic properties in order to increase the activity of the noble, non-noble metal alloys has been achieved by employing a technique in which non-noble components of the catalyst are selectively dealloyed (electrochemically dissolved) from the surface of the ORR electrocatalysts [177–179]. Dealloying and selective dissolution of Cu from the near surface of Pt-Cu bimetallic nanoparticle alloys produces a Pt-rich catalyst surface, while Cu remains present in the core region. The dealloyed Pt-Cu electrocatalyst showed enhanced activity by a factor of 4–6 at 0.9 V over a pure Pt catalyst for the ORR [177]. Further, the enhanced ORR catalytic activity of the dealloyed catalyst was related to the electronic and geometric atomic arrangement effects and to the reduced Pt–Pt interatomic distances on the surface, which is in agreement with earlier theoretical studies [180,181].

These studies revealed a correlation between the atomic environment of the bimetallic Pt-Cu surface and observed dealloying voltammetric patterns. DFT calculations showed a proximity in dissolution potentials of the bulk Cu and primarily Cu-coordinated Cu surface atoms, while higher dissolution potentials were observed for Cu atoms surrounded by Pt atoms. The authors attributed the observed voltammetric profiles of Cu dissolution to metal-specific interactions as well as kinetics of metal dissolution and surface diffusion [182].

A comparative stability study of bimetallic ($Pt_{25}Cu_{75}$) [177], and trimetallic ($Pt_{20}Co_{20}Cu_{60}$) [178], nanoparticle electrocatalysts, prepared by the electrochemical dealloying technique, were also conducted [183]. Both nanoparticle electrocatalysts showed improved resistance against electrochemical surface area loss (ECSA) in comparison to available commercial Pt electrocatalysts. XRD analysis showed that upon increasing annealing temperatures the mean particle size of the catalyst increases, which triggers lower ECSA loss. Even though the trimetallic catalyst showed improved durability based upon short term cycling, the bimetallic electrocatalyst showed superior durability in the tests performed in a MEA over extended cycling. The experimental results ruled out the stabilizing effect of Co in the trimetallic catalyst over the electrochemically dealloyed bimetallic electrocatalyst. The increased resistance toward ECSA loss, as well as specific activity improvements, resulted from increased catalyst particle sizes during cycling. Therefore, electrocatalysts were obtained with the ability to maintain their mass activity superiority over Pt/C even after extended cycling tests (30,000 voltammetric cycles) performed on the membrane (in the membrane electrode assembly fuel cell) [183].

Stamenkovic et al. studied bimetallic polycrystalline alloy films of $Pt_3M$ (where M = Ni, Co, Fe, Ti) in 0.1 M $HClO_4$ to understand the role of the 3d metals in electrocatalytic activity of Pt in ORR [184]. A volcano-type behavior was observed in the electrocatalytic activity of these alloys (peaking at $Pt_3Co$); the later transition metals, Ni, Co, and Fe, showed a large enhancement in activity when compared to the pure Pt electrode, while the enhancement was smaller for earlier transition metals. After electrochemical analysis, a Pt skin layer remained present on the surface of each bimetallic system. This volcano-behavior was found to be in strong agreement with DFT studies done by Nørskov et al. [7].

In the theoretical studies, a kinetic model was developed for bimetallic Pt electrodes alloyed with 3d transition metals that gave the rate of ORR at a certain potential as a function of the oxygen chemisorption energy, $\Delta E_O$. In this model, metals which bound oxygen too strongly caused the reaction to be limited by the removal of adsorbed oxygen species. This corresponded to a less reactive, oxidized surface, previously suggested by Ross et al. [185,186]. When metal surfaces bound the oxygen too weakly, the dissociation of oxygen (or possibly transfer of electrons and protons to the adsorbed oxygen) hindered the rate of the reaction. These two different rate-limiting steps are associated with two different mechanisms of ORR: either oxygen dissociation or proton/electron transfer to oxygen. As such, these two ORR mechanisms were considered in the analysis.

Fig. 17 depicts both of these mechanisms characterized by $\Delta E_O$, which gave rise to different slopes in the volcano plot and inferred the maximum activity at a $\Delta E_O$ of ca. 1.8 eV. The model predicted that Pt possesses too strong of a bond with oxygen (by about 0.2 eV). Calculated $\Delta E_O$ values for (1 1 1) surfaces of $Pt_3M$ alloys showed that the alloy surfaces formed weaker bonds with oxygen than pure Pt (Fig. 17). These modeled $Pt_3M$ alloys had pure Pt in the first layer and 50% Pt in the second layer in order to emulate the Pt-enriched surface with less Pt in subsequent layers and still retaining $Pt_3M$ stoichiometry. The predicted activities (relative to that of pure

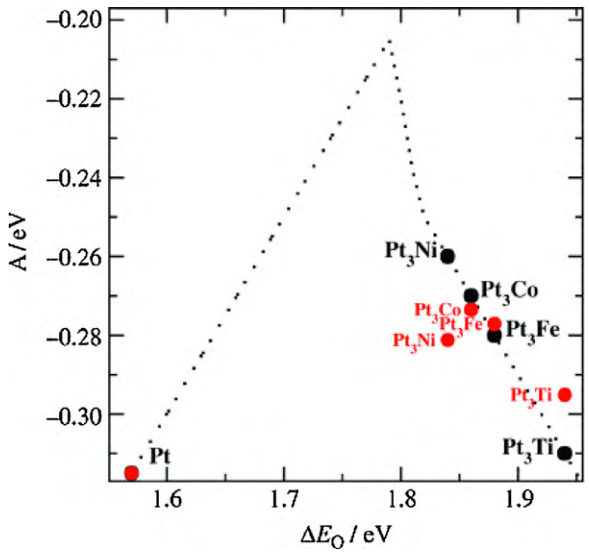


**Fig. 17.** Model of the activity at a cell potential of 0.9 V shown (. . ., ●) as a function of the adsorption energy of oxygen, $\Delta E_o$. On the left side of the plot, the rate is limited by removal of adsorbed O and OH species; immediately to the right of the maximum, the rate is limited by $O_2$ dissociation; and on the extreme right, the limiting step is protonation of adsorbed $O_2$. Also shown in red are the measured activities relative to that of Pt. The activity of the experiment is $A = k_B T \ln(i/i_{Pt}) + A_{Pt}$, where $i/i_{Pt}$ is the current density relative to Pt, and $A_{Pt}$ is the theoretical value for the activity of Pt. It is assumed that the number of active sites per surface area is the same for Pt and all the alloys. Changes in coverage for the different alloys are not considered. See text for details. Ref. [184] (with permission).

Pt) were confirmed by experimental measurements. The alloyed surfaces formed weaker bonds to oxygen than pure Pt. From the experimental results combined with theoretical models, the variation in the oxygen-metal bond strength from each metal depends on the strength of the coupling between the oxygen 2p states and the metal d states. This coupling creates bonding and anti-bonding states. The degree to which the anti-bonding states were filled dictates the strength of the interaction from surface to surface. For a metallic environment, the filling depends on the position of the states relative to the Fermi level. Therefore, an upward shift in the d states would lead to an upward shift in the anti-bonding states, which would result in less filling of the anti-bonding states and a stronger bond. The position of the d bands in each of the bimetallic electrodes was investigated via synchrotron-based high resolution photoemission spectroscopy [184] in a process reported (and already quoted) by Mun [134]. The activity of each catalyst versus the d-band center at 0.9 V (vs. RHE) showed a volcano behavior, which agreed with DFT calculations. This showed that when surfaces bound oxygen tightly, the removal of surface-oxides limited the rate. However, for surfaces that loosely bound oxygen, the transfer of electrons and protons to oxygen limited the rates of reaction.

This research [184] has explained how alloying Pt with 3d transition metals changes the electronic structure to enhance the performance of an alloy for ORR. A model of the ORR that accurately predicts trends for Pt(1 1 1) alloyed with 3d transition metal in the second layer, or for the Pt(1 1 1) overlayers on 3d metals has been proposed. From this research, a new approach has been demonstrated for screening of new catalysts for ORR by looking for surfaces which bind oxygen weaker than platinum. The activity is inferred based upon the strength of the oxygen-metal bond interaction, which depends on the position of metal d states with respect to the Fermi level. Specifically, this is accomplished by looking for surfaces with downshifts in the Pt d electronic states relative to the Fermi level.

## 5. Applications of XPS to studies of complex organic systems

### 5.1. Outline

We discuss in this section the developments of complex organic systems, both biological and nonbiological, in relation to fuel cell electrocatalysis as well as to how XPS has played a role in the experiment.

### 5.2. Metal-N4-macrocycles catalysis

Metal-N4-macrocycles, i.e., metalloporphyrins, metallocorroles, and metallophthalocyanines, have been extensively studied catalysts for the ORR [4,187–190] and are considered promising platinum-alternative electrodes. These porphyrins are relatively inexpensive and are not too difficult to synthesize. In many cases, the metalloporphyrins studied are commercially available. Studies have aimed at quantifying how selective a particular catalyst is towards the four-electron reduction of oxygen to water versus the two-electron pathway to hydrogen peroxide. The majority of these studies have been performed with water-insoluble catalysts supported on graphite electrodes immersed in aqueous solution. Fe and Co have been shown to be the most reactive species and are therefore the most studied metals incorporated into porphyrins [4,187,188]. Fe-porphyrins have been shown to be very selective towards the four electron oxygen reduction pathway. However, these metalloporphyrins are not very stable as they degrade rather quickly. Co-porphyrins show improved stability over Fe, but have a tendency to reduce oxygen via the two-electron pathway. The method for oxygen activation has been explained by molecular orbital theory [191]. Oxygen reduction is favored by partial electron transfer from the metal ion to the anti-bonding $\pi^*$ orbitals. Such backbonding can be achieved from the occupied $d_{xz}$ and $d_{yz}$ orbitals on the metal. In this bonding scheme, filled oxygen orbitals interact with the empty $d_z{}^2$ orbital on the metal. Consequently, oxygen anti-bonding $\pi^*$ orbitals lower in energy and the $d_{yz}$ and $d_{xz}$ orbitals rise in energy to interact. Cofacial porphyrins, where two porphyrins are positioned in a stacked geometry by one to four covalent linkers, have also been studied as ORR catalysts [192–194]. A co-facial bismetalloporphyrin with two cobalt atoms was observed to have a half-wave potential of 0.72 V vs. SHE and only produced 1% $H_2O_2$ [192]. The catalytic activity of cofacial bismetalloporphyrins is ascribed to bimetallic catalytic cooperativity, i.e., molecular oxygen coordinates in-between the metalloporphyrins where the oxygen is reduced via single electron steps [192,195].

Self-assembled monolayers (SAMs) of metalloporphyrins deposited on inert metal surfaces have also been studied. This approach provides for a better defined structure and film composition, and enables control of the electron transfer rate between the electrode and the deposited catalyst. XPS has been utilized in these SAM investigations, where changes in the electronic structure of the complex and oxidation state of the metal can be monitored. In one study Co(o-TMEPP), where o-TMEPP = 5,10,15,20-tetrakis[o-(2-mercaptoethoxy) phenylporphyrin, was immobilized on a gold surface [196]. XPS revealed 1 ML of surface coverage on the gold surface via an irreversible chemisorption from the thiolate moieties. Based on the sulfur BE shift, on average, three of the four thiolates attached to the porphyrin became bound to gold. This suggests a coplanar orientation of the macrocycle with respect to the surface. The films of Co(o-TMEPP) were shown to reduce oxygen via the two electron process forming hydrogen peroxide in both acidic and basic media. The Co(o-TMEPP)-coated electrode was compared to a Co-based "thioless" tetraphenyl porphine (TPP) complex. The Co(o-TMEPP) films retained catalytic activity for over $10^5$ turnovers, exceeding the activity and stability of CoTPP deposited on a graphite electrode. Later experiments [197] determined that onset of ORR corresponded to reduction to the Co(II) state and re-verified that the macrocycle is attached to the surface in a coplanar geometry.

Fe or Co-nitrogen complexes have also been investigated with respect to the ORR. The earliest method involves a physisorption treatment of a metal with a nitrogen-containing precursor, usually Fe- or Co-porphyrins, on a carbon support, whereupon pyrolysis is performed at temperatures ranging from 600 to 1000 °C, as has been reviewed extensively [4,198]. XPS surface analysis of the metal and nitrogen regions of the spectra for heat-treated Co- and Fe-porphyrins have shown fragments of the original molecule still containing the metal-nitrogen bond, while some of the original $N_4$-metal moiety is intact at lower heat-treatment temperatures [199]. Another method involves physical vapor deposition, pioneered by Dahn's group [200,201]. Combinatorial sputter deposition is performed to generate thin films of Fe (or Co) and carbon that are in the presence of $N_2$/Ar plasma. These samples are then heat-treated to induce catalytic activity. Additionally, nitrogen-rich functional groups have been grafted to a carbon black surface via a series of aminosilanes, where, after coordination of iron, the samples were pyrolyzed to induce catalytic activity [202]. From these methods, the catalytic activity depends on the amount of nitrogen present after heat-treatment. The exact structure of the active sites remains unclear. However, the active sites are believed to be composed of a metal coordinated to pyridinic- or pyrrolic-type nitrogen sites embedded into the carbon support at the edge of the basal planes [203]. Work from Dodelet's group has produced a heat-treated Fe-based catalyst that suggest the Fe bridges two graphitic sheets via nitrogen coordination [204].

Heat treated metalloporphyrins have been shown to be more active than platinum catalysts with methanol as the fuel. This methanol tolerance makes heat-treated metalloporphyrins suitable catalysts at the cathode of DMFCs. In the case of traditional platinum DMFC cathode catalysts, methanol may cross over from the anode to the cathode. At the cathode, the methanol may react with $O_2$, thereby depressing the $O_2$ surface concentration on the cathode and reducing a fuel cell efficiency. Heat-treated binary metallic catalysts (V/Fe, Co/Fe, Ni/Fe, and Cu/Fe) using TPP were tested for their ORR activities in oxygen-saturated 0.5 M sulfuric acid with 1 M methanol and compared with single heat-treated metalloporphyrins [205]. The FeTPP and CoTPP combination gave the best results, where the ORR current was measured over 2 mA $cm^{-2}$. This value was measurably higher than FeTPP or CoTPP (ca 1.0 mA $cm^{-2}$). The enhanced activity of the FeTPP/CoTPP system was attributed to bimetallic cooperativity, as discussed in the cofacial porphyrin research [192,193,195].

### 5.3. Biocatalysis

Biological fuel cells (enzymatic biofuel cells) are a growing and important area of research [206,207]. Although their total powers are orders of magnitude lower (ca. $10^{-7}$ to $10^{-3}$ W) than those of the fuel cells previously discussed, they find applications in electronic devices requiring low currents, e.g., in cardiac pacemakers and in self-powering sensors for monitoring blood glucose levels [206]. The enzymes used in most of the investigations are electrically connected to electrodes through electron conducting hydrogels [208].

Different analytical techniques are required to characterize enzymatic biofuel cells. XPS has been applied in experiments to monitor the attachment of proteins to the electrode as well as to determine the elemental catalyst compositions [209–211]. Additionally, angle-resolved XPS has been used for determining the structure of individual layers of a layer by layer deposited enzyme [212]. In one particular study, direct electrocatalysis of glucose was demonstrated by entrapping glucose oxidase in a silica/carbon

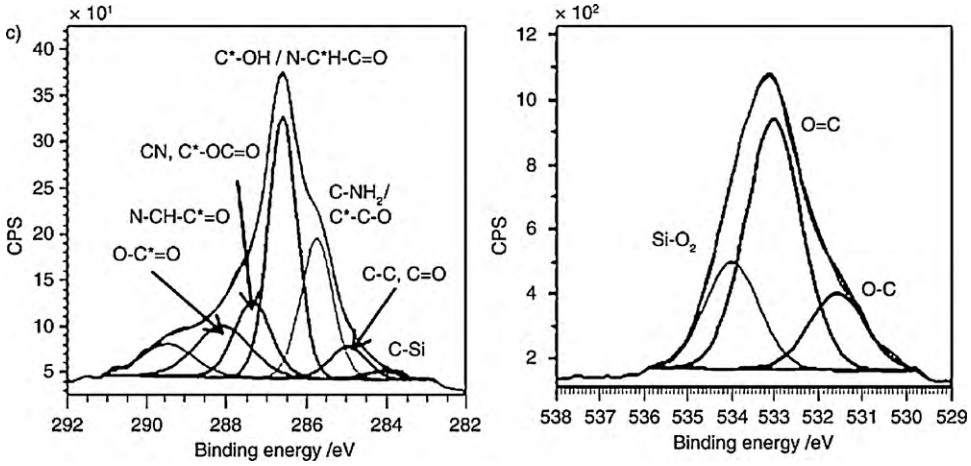


**Fig. 18.** XPS spectra silica composites with entrapped glucose oxidase and carbon nanotubes. The C1s spectrum of glucose oxidase has three main peaks corresponding to the following bonds: aliphatic C*H—CH (284.8 eV) that may have originated from surface contamination, oxydrilic C*—OH and amidic N—C*H—CO (286.6 eV), and N—CH—C*=O (288.3 eV), where the respective carbon species are marked by an asterisk. Ref. [213] (with permission).

nanotube composite obtained through the lysozyme-catalyzed synthesis of silica [213]. The C(1s) spectrum of the silica composite contains features of both enzymes (Fig. 18). The peak at 286.6 eV corresponds to spectra for glucose oxidase, and a secondary signal at 285.8 eV corresponds to the primary peak in the spectra of lysozyme. High resolution O(1s) spectra also confirm the presence of immobilized enzymes from the BE at 533 eV, attributed to C=O. Furthermore, the conversion of a chemical precursor (tetramethylorthosilicate) to silica is confirmed by silicon in the oxygen spectra. The immobilization method studied facilitates mediator-free direct electron transfer coupled to the oxidation of glucose on a conductive matrix that stabilized enzyme activity for periods of at least 1 month. Direct electron transfer between the enzyme and the electrode, whereby electron mediators are not utilized, has the greatest potential for miniaturization and high power output. Work such as this paves the way for biofuel cells for use in fuel cell devices.

Microbial fuel cells (MFC) use microorganisms with the ability to harness electricity and provide energy for their growth by oxidizing organic materials [214]. XPS has been employed to analyze the surfaces of electrodes in order to detect the formation of oxidation products. Permanganate as the cathodic electron acceptor in both acidic and alkaline conditions was employed in an MFC, and the conversion of permanganate to $MnO_2$ was confirmed by the binding energy peaks of Mn $2p_{1/2}$ (654.03 eV) and Mn $2p_{3/2}$ (642.6 eV) [214]. Because of the high cathodic redox potential of permanganate, this type of MFC displayed a higher power-output (115.60 mW $m^{-2}$) relative to systems incorporating more conventional cathodic electron acceptors, i.e. hexacyanoferrate (25.62 mW $m^{-2}$) or oxygen (10.2 mW $m^{-2}$). In another instance an MFC was used to treat $Cr^{6+}$, the cathodic electron acceptor in this experiment, from electroplating waste water as well as to generate electricity [215]. The chromium ion, in the form of $Cr_2O_7^{2-}$, was reduced to $Cr_2O_3$ and precipitated on the surface of the electrode. XPS was used to monitor the precipitation, which appeared at 575.6 eV in the spectrum.

## 6. Modern developments in XPS methodology

### 6.1. A synchrotron source

Several of the publications discussed acquired XPS spectra from synchrotron sources [25,84,134,184]. Synchrotron sources utilize multi-GeV electron beams circulating around large rings of magnets in order to produce intense, bright radiation that is several orders of magnitude higher than that obtained from conventional laboratory X-ray sources. The photons may be monochromatized to obtain a very narrow energy range. The photon energy can also be tuned to allow for surface analysis at different depths, since analysis depth and surface sensitivity vary with photon energy. This aspect was highlighted in Fig. 2, where photoelectron IMFP is a function of photon energy. Experiments employing synchrotron radiation yield high resolution XPS spectra, where resolutions can be higher than 100 meV.

Fig. 19 shows the Pt 4f photoelectron spectral region of a Pt(1 1 1) surface [49]. The data were collected at an undulator beam line using a Scienta SES-2002 analyzer at 80 meV resolution. A low photon energy of 160 eV was selected in order to enhance surface sensitivity, which is one of the advantages of using the tunable synchrotron source. From the figure, it is clear that a shoulder is present on the high binding energy side of both the Pt $4f_{7/2}$ and $4f_{5/2}$ peaks, indicating the presence of multiple species. Because of the low photon energy and the presumed cleanliness of the surface, these two pairs of peaks were attributed to bulk and surface platinum atoms. The surface atoms are present at BEs of 74.30 and 70.97 eV while the bulk atoms display higher BEs at 74.92 and 71.54 eV. Surface Pt atoms display a lower binding energy

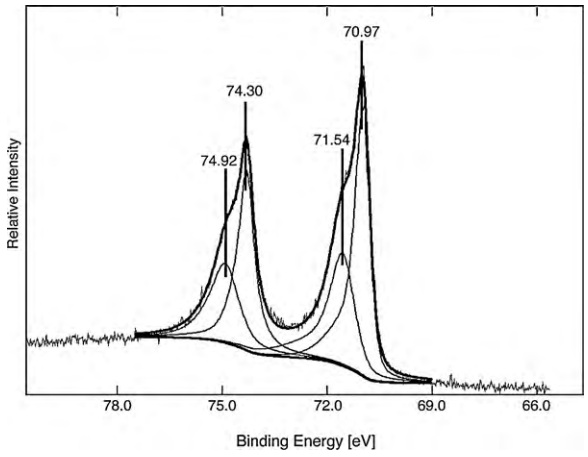


**Fig. 19.** The Pt 4f region of Pt(1 1 1) measured at 160 eV photon energy at the 80 meV resolution (from the Fermi edge). The data were collected at University of Wisconsin Synchrotron Radiation Center. A low photon energy was selected in order to achieve surface sensitivity. A shoulder is present on the high binding energy side of both the Pt $4f_{7/2}$ and $4f_{5/2}$ peaks, indicating the presence of two platinum species. Ref. [49] (with permission).

than those in the bulk because of two initial state effects arising from the lower coordination of surface compared to bulk atoms [108,166,167]. This result provides a good example of the power of the synchrotron photoelectron spectroscopy technique in the study of surfaces, which are of particular importance to heterogeneous catalysis.

### 6.2. Ambient pressure photoelectron spectroscopy

A novel XPS technique is the ambient pressure photoelectron spectroscopy (APPES). APPES, also known as APXPS or high-pressure XPS (HPXPS), enables the analysis of surface electronic structure between the gas-solid interface at pressures and temperatures that were previously impossible [216]. This technique helps fill the "pressure gap" associated with surface studies done under UHV conditions. The pressure gap between UHV and a few-Torr range, may be as high as ten orders of magnitude [29,30]. Recently developed APPES instruments incorporate an electrostatic lens focused onto a differential pumping scheme. This technology enables the collection of a greater fraction of photoelectrons that would be lost due to electron scattering under non-UHV conditions. The spectroscopy is applicable in environmental science, catalysis, as well as in other surface-oriented sciences. For recent, extremely thorough reviews of APPES and other high pressure techniques, readers may look at Refs. [216,217].

### 6.3. Improvements to laboratory instruments

Gelius and colleagues have developed a water-cooled rotating anode device which possesses higher brightness than conventional fixed-anode sources [218]. With this device, the FWHM resolution from the Fermi edge of Ag was 0.27 eV. Advances in XPS equipment have also come from more powerful electron energy analyzers [219]. An ellipsoidal display analyzer has been developed for angle-resolved XPS measurements and related techniques; where it measures the angle-resolved intensity of photoelectrons at fixed energy [220]. The large acceptance angle of this device provides for a collection efficiency greater than standard hemispherical analyzers. An analyzer called the hyperbolic field analyzer [221] as well as a parallel cylindrical mirror analyzer [222] have also been developed. The resolutions provided from these analyzers, however, are suitable for AES measurements but do not meet the resolution demands for XPS. These multi-channel analyzers can measure a wide distribution of electron energies over a large range of directions, hence making possible angle resolved photoemission. The principle advantage of these and other multi-channel analyzers is that they reduce measurement time, avoiding potential sample degradation. Analyzers are expected to gradually improve based upon using multi-channel electron detectors [223,224].

### 6.4. The use of lasers

Infrared, visible, and UV lasers have been employed to heat plasma in order to create X-rays [225,226]. One study employed this line-focused laser irradiation technique to produce a XPS spectrum of silicon with an energy resolution of 2 eV and a spatial resolution of 20 μm [225]. While the energy resolution is not as high compared to laboratory instruments, the spatial resolution is much more powerful. This high spatial resolution can be applicable in studies where a small surface area can be analyzed, such as microchip fabrication. Currently there are no X-ray lasers that are powerful enough for XPS studies with great resolution. Single-pass free-electron lasers that operate upon self-amplified spontaneous emission provide another source for X-ray lasers [227]. These devices could produce high X-ray photon fluxes in short laser-like pulses.

Additionally, from a publication in the late 1990s, a compact laser storage ring has been developed for electron beam cooling or generating X-rays based on Compton scattering [228]. This compact light source is the size of a large desk and stores electrons at far lower energies, roughly 25 MeV compared to the several-GeV energy range of synchrotron sources [229]. The device has been designed for the hard X-ray range (5 to 35 keV), with the brightness being several orders lower than that achieved by synchrotrons [229]. These higher X-ray energies are not a limitation for surface analysis, as surface sensitivity may be enhanced based upon grazing-emission angles [19].

## 7. Conclusions

We have demonstrated how XPS can be employed to acquire information about electrocatalysts for fuel cell applications. In the perspective of the reviewed research, theoretical models along with XPS and other experimental data work were used in tandem to provide a more comprehensive understanding of the electrochemical behavior found at the surfaces of electrocatalysts. The characterization of fuel cell catalysts is important for the understanding, exploration, and development of new, potent fuel cell catalysts. A combination of *in situ* and *ex situ* electrochemical techniques with XPS will enable detailed characterization of catalytic systems. Beyond the use of commercial XPS instruments, synchrotron-based light sources can be utilized to achieve high-resolution XPS spectra. These high-resolution spectra may contain information that might not have been present at a lower resolution. XPS can serve as an analytical tool for quantifying adsorbed species as well as measurement of chemical states at the topmost layers of the material. This aspect was demonstrated in monitoring the formation of thin films deposited on metallic surfaces as well as studies concerning the electrolyte/electrode interface, and determining the role of ruthenium on platinum-ruthenium bimetallic catalysts. Further, from the chemical shift, XPS yields information about the surface electronic structure. This has come from studies of catalysts outlined in Section 4. Proposed models explaining certain trends in BE shifts, e.g., the d-band center theory, have proven powerful tools for predicting and determining the activity at the surface of metals, and this feature can be monitored via XPS.

## Acknowledgements

This work was supported by the National Science Foundation under grant NSF CHE 06-51083 and by the Army Research Office grant: Army W911NF-08-1. Partial support of this project by DOE LANL 53183-0 is also appreciated. One of us, P.S.B., wishes to acknowledge additional support from the Geosciences Research Program, Office of Basic Energy Sciences, U.S. DOE. Computer support from the Pittsburgh Supercomputer Center is also acknowledged.

## References

[1] I. EG&G Technical Services, Fuel Cell Handbook, 7th ed., U.S. Dept. of Energy, National Energy Technology Laboratory, Strategic Center for Natural Gas, Morgantown, WV, 2004.
[2] W. Vielstich, A. Lamm, H.A. Gasteiger, Handbook of Fuel Cells: Fundamentals, Technology, and Applications, Wiley, Chichester, England; Hoboken, NJ, 2003.
[3] N.M. Markovic, P.N. Ross, Surf. Sci. Rep. 45 (2002) 121–229.
[4] J.H. Zagal, F. Bedioui, J.P. Dodelet, N4-Macrocyclic Metal Complexes, Springer, New York, 2006.
[5] W. Chrzanowski, A. Wieckowski, in: A. Wieckowski (Ed.), Interfacial Electrochemistry—Theory, Experiment, and Applications, Marcel Dekker, Inc, New York, 1999, pp. 937–954.
[6] B. Hammer, Y. Morikawa, J.K. Norskov, Phys. Rev. Lett. 76 (1996) 2141–2144.
[7] J.K. Norskov, J. Rossmeisl, A. Logadottir, L. Lindqvist, J.R. Kitchin, T. Bligaard, H. Jonsson, J. Phys. Chem. B 108 (2004) 17886–17892.

[8] B. Hammer, J.K. Norskov, Surf. Sci. 343 (1995) 211–220.
[9] J.R. Kitchin, J.K. Norskov, M.A. Barteau, J.G. Chen, Phys. Rev. Lett. 93 (2004) 156801.
[10] B. Richter, H. Kuhlenbeck, H.J. Freund, P.S. Bagus, Phys. Rev. Lett. 93 (2004) 026805.
[11] J.A. Rodriguez, D.W. Goodman, Science 257 (1992) 897–903.
[12] J.A. Rodriguez, Surf. Sci. Rep. 24 (1996) 225–287.
[13] Y.Y. Tong, H.S. Kim, P.K. Babu, P. Waszczuk, A. Wieckowski, E. Oldfield, J. Am. Chem. Soc. 124 (2002) 468–473.
[14] K. Siegbahn, C. Nordling, A. Fahlman, R. Nordberg, K. Hamrin, J. Hedman, G. Johansson, T. Bergmark, S.E. Karlsson, I. Lindgren, B. Lindberg, ESCA-Atomic, Molecular, and Solid State Structure Studied by Means of Electron Spectroscopy, Almqvist and Wiksells, Uppsala, Sweden, 1967.
[15] K. Siegbahn, C. Nordling, G. Johansson, J. Hedman, P.F. Hedén, K. Hamrin, U. Gelius, T. Bergmark, L.O. Werme, R. Manne, Y. Baer, ESCA-Applied to Free Molecules, North-Holland, Amsterdam, 1969.
[16] J. Stöhr, in: G. Ertl, R. Gomer, D.L. Mills (Eds.), Springer Series in Surface Sciences, Vol. 25, Springer-Verlag, Berlin, 1996.
[17] P. Mrozek, M. Han, Y.E. Sung, A. Wieckowski, Surf. Sci. 319 (1994) 21–33.
[18] P. Mrozek, Y.E. Sung, M. Han, M. Gamboaaldeco, A. Wieckowski, C.H. Chen, A.A. Gewirth, Electrochim. Acta 40 (1995) 17–28.
[19] C.S. Fadley, Prog. Surf. Sci. 16 (1984) 275–388.
[20] A. Baraldi, G. Comelli, S. Lizzit, M. Kiskinova, G. Paolucci, Surf. Sci. Rep. 49 (2003) 169–224.
[21] P.S. Bagus, A. Wieckowski, H. Freund, Chem. Phys. Lett. 420 (2006) 42–46.
[22] P.S. Bagus, C. Woll, A. Wieckowski, Surf. Sci. 603 (2009) 273–283.
[23] A. Lewera, W.P. Zhou, R. Hunger, W. Jaegermann, A. Wieckowski, S. Yockel, P.S. Bagus, Chem. Phys. Lett. 447 (2007) 39–43.
[24] A. Lewera, W.P. Zhou, C. Vericat, J.H. Chung, R. Haasch, A. Wieckowski, P.S. Bagus, Electrochim. Acta 51 (2006) 3950–3956.
[25] M.A. Rigsby, W.P. Zhou, A. Lewera, H.T. Duong, P.S. Bagus, W. Jaegermann, R. Hunger, A. Wieckowski, J. Phys. Chem. C 112 (2008) 15595–15601.
[26] C. Vericat, M. Wakisaka, R. Haasch, P.S. Bagus, A. Wieckowski, J. Solid State Electrochem. 8 (2004) 794–803.
[27] W.P. Zhou, A. Lewera, P.S. Bagus, A. Wieckowski, J. Phys. Chem. C 111 (2007) 13490–13496.
[28] W.P. Zhou, A. Lewera, R. Larsen, R.I. Masel, P.S. Bagus, A. Wieckowski, J. Phys. Chem. B 110 (2006) 13393–13398.
[29] H. Bluhm, D.F. Ogletree, C.S. Fadley, Z. Hussain, N. Salmeron, J. Phys. -Condes. Matter 14 (2002) L227–L233.
[30] H. Bluhm, M. Havecker, A. Knop-Gericke, M. Kiskinova, R. Schlogl, M. Salmeron, MRS Bull. 32 (2007) 1022–1030.
[31] T.L. Barr, Modern ESCA: The Principles and Practice of X-Ray Photoelectron Spectroscopy, CRC Press, Boca Raton, 1994.
[32] C.S. Fadley, Surf. Interface Anal. 40 (2008) 1579–1605.
[33] P.S. Bagus, K. Hermann, Phys. Rev. B 33 (1986) 2987–2991.
[34] P.S. Bagus, C.J. Nelin, K. Hermann, Aust. J. Phys. 39 (1986) 731–747.
[35] P.S. Bagus, F. Illas, G. Pacchioni, F. Parmigiani, J. Electron Spectrosc. Relat. Phenom. 100 (1999) 215–236.
[36] P.S. Bagus, E.S. Ilton, Phys. Rev. B 73 (2006) 155110–155111.
[37] E.S. Ilton, P.S. Bagus, Surf. Sci. 602 (2008) 1114–1121.
[38] P.S. Bagus, D. Coolbaugh, S.P. Kowalczyk, G. Pacchioni, F. Parmigiani, J. Electron. Spectrosc. Relat. Phenom. 51 (1990) 69–74.
[39] P.S. Bagus, R. Broer, W.A. de Jong, W.C. Nieuwpoort, F. Parmigiani, L. Sangaletti, Phys. Rev. Lett. 84 (2000) 2259–2262.
[40] N.W. Ashcroft, N.D. Mermin, Solid State Physics, Holt, Rinehart, and Winston, NY, 1976.
[41] D. Briggs, J.T. Grant, IM Publications and Surface Spectra Ltd., Charlton and Manchester, 2003.
[42] C.J. Powell, A. Jablonski, Nucl. Instrum. Methods Phys. Res., Sect. A 601 (2009) 54–65.
[43] S. Tanuma, C.J. Powell, D.R. Penn, Surf. Interface Anal. 37 (2005) 1–14.
[44] G.A. Somorjai, Introduction to Surface Chemistry and Catalysis, Wiley, New York, 1994.
[45] R. Nyholm, J.N. Andersen, J.F. van Acker, M. Qvarford, Phys. Rev. B 44 (1991) 10987–10990.
[46] D.A. Shirley, Phys. Rev. B 5 (1972) 4709–4714.
[47] M.P. Seah, Surf. Sci. 420 (1999) 285–294.
[48] M.P. Seah, I.S. Gilmore, S.J. Spencer, Surf. Sci. 461 (2000) 1–15.
[49] M.A. Rigsby, A combined electrochemical and X-ray photoelectron spectroscopic approach to electrocatalysis (Ph.D. thesis), University of Illinois at Urbana-Champaign, Urbana, 2010.
[50] P.S. Bagus, M. Schrenk, D.W. Davis, D.A. Shirley, Phys. Rev. A 9 (1974) 1090–1096.
[51] L. Sangaletti, F. Parmigiani, P.S. Bagus, Phys. Rev. B 66 (2002) 115106.
[52] J.H. Scofield, J. Electron, Spectrosc. Relat. Phenom. 8 (1976) 129–137.
[53] J.J. Yeh, I. Lindau, At. Data Nucl. Data Tables 32 (1985) 1–155.
[54] T. Åberg, Phys. Rev. 156 (1967) 35–41.
[55] R. Manne, T. Aberg, Chem. Phys. Lett. 7 (1970) 282–284.
[56] W.L. Jolly, D.N. Hendrickson, J. Am. Chem. Soc. 92 (1970) 1863–1871.
[57] D.P. Chong, O.V. Gritsenko, E.J. Baerends, J. Chem. Phys. 116 (2002) 1760–1772.
[58] P.S. Bagus, Phys. Rev. 139 (1965) A619.
[59] P.S. Bagus, E.K. Viinikka, Phys. Rev. A 15 (1977) 1486–1496.
[60] D.P. Chong, J. Chem. Phys. 103 (1995) 1842–1845.
[61] W.F. Egelhoff, Surf. Sci. Rep. 6 (1987) 253–415.
[62] C.D. Wagner, J. Electron Spectrosc. Relat. Phenom. 10 (1977) 305–315.
[63] G. Hohlneicher, H. Pulm, H.J. Freund, J. Electron Spectrosc. Relat. Phenom. 37 (1985) 209–224.
[64] J. Hedman, P.F. Hedén, C. Nordling, K. Siegbahn, Phys. Lett. A 29 (1969) 178–179.
[65] R.P. Gupta, S.K. Sen, Phys. Rev. B 10 (1974) 71–77.
[66] R.P. Gupta, S.K. Sen, Phys. Rev. B 12 (1975) 15–19.
[67] P.S. Bagus, R. Broer, E.S. Ilton, Chem. Phys. Lett. 394 (2004) 150–154.
[68] P.S. Bagus, R. Broer, E.S. Ilton, J. Electron Spectrosc. Relat. Phenom. 165 (2008) 46–49.
[69] E.S. Ilton, J.-F. Boily, P.S. Bagus, Surf. Sci. 601 (2007) 908.
[70] C.R. Brundle, P.S. Bagus, D. Menzel, K. Hermann, Phys. Rev. B 24 (1981) 7041–7056.
[71] F.M.F. de Groot, J. Electron Spectrosc. Relat. Phenom. 67 (1994) 529–622.
[72] P.S. Bagus, F. Illas, in: P.v.R. Schleyer, N.L. Allinger, T. Clark, J. Gasteiger, P.A. Kollman, H.F. Schaefer (Eds.), Encyclopedia of Computational Chemistry, Wiley, Chichester, United Kingdom, 1998, pp. 2870–2887.
[73] J. Stöhr, NEXAFS Spectroscopy, Springer-Verlag, Berlin, 1992.
[74] J.A. Gubner, J. Phys. A: Math. Gen. 27 (1994) 745–749.
[75] J.E. Castle, H. Chapman-Kpodo, A. Proctor, A.M. Salvi, J. Electron Spectrosc. Relat. Phenom. 106 (2000) 65–80.
[76] C.J. Powell, J.M. Conny, Surf. Interface Anal. 41 (2009) 269–294.
[77] N. Fairley, CasaXPS, 2.3.9 ed., Casa Software Ltd., Teighnmouth, 2003.
[78] A.T. Hubbard, Acc. Chem. Res. 13 (1980) 177–184.
[79] D.C. Zapien, J.Y. Gui, D.A. Stern, A.T. Hubbard, J. Electroanal. Chem. 330 (1992) 469–487.
[80] M. Wakisaka, S. Mitsui, Y. Hirose, K. Kawashima, H. Uchida, M. Watanabe, J. Phys. Chem. B 110 (2006) 23489–23496.
[81] P.A. Thiel, T.E. Madey, Surf. Sci. Rep. 7 (1987) 211–385.
[82] M.A. Henderson, Surf. Sci. Rep. 46 (2002) 5–308.
[83] D.L. Doering, T.E. Madey, Surf. Sci. 123 (1982) 305–337.
[84] H. Ogasawara, B. Brena, D. Nordlund, M. Nyberg, A. Pelmenschikov, L.G.M. Pettersson, A. Nilsson, Phys. Rev. Lett. 89 (2002) 276102.
[85] W. Eberhardt, Application of Synchroton Radiation; High Resolution Studies of Molecules and Molecular Adsorbates, Springer, Berlin, 1995.
[86] M.P. Soriaga, Chem. Rev. 90 (1990) 771–793.
[87] G.M. Berry, M.E. Bothwell, B.G. Bravo, G.J. Cali, J.E. Harris, T. Mebrahtu, S.L. Michelhaugh, J.F. Rodriguez, M.P. Soriaga, Langmuir 5 (1989) 707–713.
[88] B.G. Bravo, S.L. Michelhaugh, M.P. Soriaga, I. Villegas, D.W. Suggs, J.L. Stickney, J. Phys. Chem. 95 (1991) 5245–5249.
[89] A.T. Hubbard, Chem. Rev. 88 (1988) 633–656.
[90] A. Wieckowski, S.D. Rosasco, B.C. Schardt, J.L. Stickney, A.T. Hubbard, Inorg. Chem. 23 (1984) 565–569.
[91] J.L. Stickney, S.D. Rosasco, G.N. Salaita, A.T. Hubbard, Langmuir 1 (1985) 66–71.
[92] J.L. Stickney, S.D. Rosasco, A.T. Hubbard, J. Electrochem. Soc. 131 (1984) 260–267.
[93] S.K. Jo, J.M. White, Surf. Sci. 261 (1992) 111–117.
[94] P.A. Bennett, J.C. Fuggle, Phys. Rev. B 26 (1982) 6030–6039.
[95] P. Babu, E. Oldfield, A. Wieckowski, Modern Aspects of Electrochemistry, Kluwer Academic Publishers, New York, 2002, pp. 1–48.
[96] G.Q. Lu, A. Crown, A. Wieckowski, J. Phys. Chem. B 103 (1999) 9700–9711.
[97] Y.X. Chen, M. Heinen, Z. Jusys, R.B. Behm, Angew. Chem. Int. Ed. 45 (2006) 981–985.
[98] R. Ianniello, V.M. Schmidt, U. Stimming, J. Stumper, A. Wallau, Electrochim. Acta 39 (1994) 1863–1869.
[99] X.M. Ren, P. Zelenay, S. Thomas, J. Davey, S. Gottesfeld, J. Power Sources 86 (2000) 111–116.
[100] S.C. Thomas, X.M. Ren, S. Gottesfeld, P. Zelenay, Electrochim. Acta 47 (2002) 3741–3748.
[101] O.A. Petrii, J. Solid State Electrochem. 12 (2008) 609–642.
[102] T.D. Jarvi, T.H. Madden, E.M. Stuve, Electrochem. Solid-State Lett. 2 (1999) 224–227.
[103] E. Herrero, J.M. Feliu, A. Wieckowski, Langmuir 15 (1999) 4944–4948.
[104] A. Crown, H. Kim, G.Q. Lu, I.R. de Moraes, C. Rice, A. Wieckowski, J. New Mater. Electrochem. Syst. 3 (2000) 275–284.
[105] J.B. Goodenough, A. Hamnett, B.J. Kennedy, R. Manoharan, S.A. Weeks, J. Electroanal. Chem. 240 (1988) 133–145.
[106] A. Hamnett, B.J. Kennedy, Electrochim. Acta 33 (1988) 1613–1618.
[107] H. Kim, I.R. de Moraes, G. Tremiliosi, R. Haasch, A. Wieckowski, Surf. Sci. 474 (2001) L203–L212.
[108] F. Maillard, G.Q. Lu, A. Wieckowski, U. Stimming, J. Phys. Chem. B 109 (2005) 16230–16243.
[109] H.A. Gasteiger, N. Markovic, P.N. Ross, E.J. Cairns, J. Phys. Chem. 97 (1993) 12020–12029.
[110] T. Yajima, H. Uchida, M. Watanabe, J. Phys. Chem. B 108 (2004) 2654–2659.
[111] N.M. Markovic, H.A. Gasteiger, P.N. Ross, X.D. Jiang, I. Villegas, M.J. Weaver, Electrochim. Acta 40 (1995) 91–98.
[112] W. Chrzanowski, H. Kim, A. Wieckowski, Catal. Lett. 50 (1998) 69–75.
[113] M. Watanabe, Y.M. Zhu, H. Igarashi, H. Uchida, Electrochemistry 68 (2000) 244–251.
[114] D. Kardash, C. Korzeniewski, N. Markovic, J. Electroanal. Chem. 500 (2001) 518–523.
[115] D. Cao, G.Q. Lu, A. Wieckowski, S.A. Wasileski, M. Neurock, J. Phys. Chem. B 109 (2005) 11622–11633.
[116] C. Lu, C. Rice, R.I. Masel, P.K. Babu, P. Waszczuk, H.S. Kim, E. Oldfield, A. Wieckowski, J. Phys. Chem. B 106 (2002) 9581–9589.

[117] H.A. Gasteiger, N. Markovic, P.N. Ross, E.J. Cairns, J. Electrochem. Soc. 141 (1994) 1795–1803.
[118] P. Waszczuk, G.Q. Lu, A. Wieckowski, C. Lu, C. Rice, R.I. Masel, Electrochim. Acta 47 (2002) 3637–3652.
[119] C. Rice, R.I. Ha, R.I. Masel, P. Waszczuk, A. Wieckowski, T. Barnard, J. Power Sources 111 (2002) 83–89.
[120] P. Waszczuk, T.M. Barnard, C. Rice, R.I. Masel, A. Wieckowski, Electrochem. Commun. 4 (2002) 599–603.
[121] C. Rice, S. Ha, R.I. Masel, A. Wieckowski, J. Power Sources 115 (2003) 229–235.
[122] M.C. Zhao, C. Rice, R.I. Masel, P. Waszczuk, A. Wieckowski, J. Electrochem. Soc. 151 (2004) A131–A136.
[123] Y.M. Zhu, S.Y. Ha, R.I. Masel, J. Power Sources 130 (2004) 8–14.
[124] S. Ha, R. Larsen, R.I. Masel, J. Power Sources 144 (2005) 28–34.
[125] S. Ha, Z. Dunbar, R.I. Masel, J. Power Sources 158 (2006) 129–136.
[126] R. Larsen, S. Ha, J. Zakzeski, R.I. Masel, J. Power Sources 157 (2006) 78–84.
[127] Y.X. Chen, M. Heinen, Z. Jusys, R.J. Behm, Langmuir 22 (2006) 10399–10408.
[128] Y.X. Chen, S. Ye, M. Heinen, Z. Jusys, M. Osawa, R.J. Behm, J. Phys. Chem. B 110 (2006) 9534–9544.
[129] G. Comelli, M. Sastry, G. Paolucci, K.C. Prince, L. Olivi, Phys. Rev. B 43 (1991) 14385–14389.
[130] D. Hennig, M.V. Ganduglia-Pirovano, M. Scheffler, Phys. Rev. B 35 (1996) 10344–10347.
[131] J.A. Rodriguez, R.A. Campbell, D.W. Goodman, J. Vac. Sci. Technol., A 10 (1992) 2540–2545.
[132] R.Q. Wu, A.J. Freeman, Phys. Rev. B 52 (1995) 12419–12425.
[133] V. Pallassana, M. Neurock, L.B. Hansen, B. Hammer, J.K. Norskov, Phys. Rev. B 60 (1999) 6146–6154.
[134] B.S. Mun, C. Lee, V. Stamenkovic, N.M. Markovic, P.N. Ross, Phys. Rev. B 71 (2005) 6.
[135] J.N. Andersen, D. Hennig, E. Lundgren, M. Methfessel, R. Nyholm, M. Scheffler, Phys. Rev. B 50 (1994) 17525–17533.
[136] J.S. Kang, D.W. Hwang, J.H. Hong, J.I. Jeong, H.K. An, Y.P. Lee, J.J. Lee, K.H. Kim, J. Magnet. Magnet. Mater. 150 (1995) 323–328.
[137] B. Hammer, J.K. Norskov, in: B.C. Gates, H. Knozinger (Eds.), Advances in Catalysis, Vol. 45, Academic Press Inc, San Diego, 2000, pp. 71–129.
[138] W.P. Zhou, L.A. Kibler, D.M. Kolb, Electrochim. Acta 49 (2004) 5007–5012.
[139] J.M. Feliu, A. Fernandezvega, A. Aldaz, J. Clavilier, J. Electroanal. Chem. 256 (1988) 149–163.
[140] J. Clavilier, J.M. Feliu, A. Fernandezvega, A. Aldaz, J. Electroanal. Chem. 294 (1990) 193–208.
[141] L. Dollard, R.W. Evans, G.A. Attard, J. Electroanal. Chem. 345 (1993) 205–221.
[142] M.K. Bahl, R.O. Woodall, R.L. Watson, K.J. Irgolic, J. Chem. Phys. 64 (1976) 1210–1218.
[143] J.A. Taylor, J. Vac. Sci. Technol. 20 (1982) 751–755.
[144] W.J. Stec, J.R. Vanwazer, W.E. Morgan, R.G. Albridge, Inorg. Chem. 11 (1972) 219.
[145] W.P. Zhou, L.A. Kibler, D.M. Kolb, Electrochim. Acta 47 (2002) 4501–4510.
[146] J.B. Goodenough, A. Hamnett, B.J. Kennedy, S.A. Weeks, Electrochim. Acta 32 (1987) 1233–1238.
[147] R. Van Hardeveld, A. Van Montfoort, Surf. Sci. 4 (1966) 396–430.
[148] K.S. Kim, N. Winograd, R.E. Davis, J. Am. Chem. Soc. 93 (1971) 6296.
[149] G.C. Allen, P.M. Tucker, A. Capon, R. Parsons, J. Electroanal. Chem. 50 (1974) 335–343.
[150] A. Katayama, J. Phys. Chem. 84 (1980) 376–381.
[151] J.S. Hammond, N. Winograd, Comprehensive Treastise in Electrochemistry, Plenum Press, New York, 1984.
[152] A. Shukla, K.V. Ramesh, R. Manoharan, P.R. Sarode, T. Vasudevan, Ber. Bunsen Ges. Phys. Chem. 89 (1985) 1261.
[153] K.W. Park, J.H. Choi, B.K. Kwon, S.A. Lee, Y.E. Sung, H.Y. Ha, S.A. Hong, H. Kim, A. Wieckowski, J. Phys. Chem. B 106 (2002) 1869–1877.
[154] K.L. Ley, R.X. Liu, C. Pu, Q.B. Fan, N. Leyarovska, C. Segre, E.S. Smotkin, J. Electrochem. Soc. 144 (1997) 1543–1548.
[155] H.F. Oetjen, V.M. Schmidt, U. Stimming, F. Trila, J. Electrochem. Soc. 143 (1996) 3838–3842.
[156] L.V. Interrante, M.J. Hampden-Smith, Chemistry of Advanced Materials: An Overview, Wiley-VCH, New York, 1998.
[157] K. Lee, O. Savadogo, A. Ishihara, S. Mitsushima, N. Kamiya, K. Ota, J. Electrochem. Soc. 153 (2006) A20–A24.
[158] A.K. Shukla, R.K. Raman, K. Scott, Fuel Cells 5 (2005) 436–447.
[159] E.J. Biddinger, U.S. Ozkan, Top. Catal. 46 (2007) 339–348.
[160] P.H. Matter, U.S. Ozkan, Catal. Lett. 109 (2006) 115–123.
[161] M. Weinert, R.E. Watson, Phys. Rev. B 51 (1995) 17168–17180.
[162] H. Uchida, H. Ozuka, M. Watanabe, Electrochim. Acta 47 (2002) 3629–3636.
[163] B. Johansson, N. Martensson, Phys. Rev. B 21 (1980) 4427–4457.
[164] M.L. Shek, P.M. Stefan, C. Binns, I. Lindau, W.E. Spicer, Surf. Sci. 115 (1982) L81–L85.
[165] O. Bjorneholm, A. Nilsson, H. Tillborg, P. Bennich, A. Sandell, B. Hernnas, C. Puglia, N. Martensson, Surf. Sci. 315 (1994) L983–L989.
[166] P.S. Bagus, C.R. Brundle, G. Pacchioni, F. Parmigiani, Surf. Sci. Rep. 19 (1993) 265–283.
[167] P.S. Bagus, G. Pacchioni, Phys. Rev. B 48 (1993) 15274.
[168] G.F. Cabeza, P. Legare, N.J. Castellani, Surf. Sci. 465 (2000) 286–300.
[169] S. Mukerjee, S. Srinivasan, J. Electroanal. Chem. 357 (1993) 201–224.
[170] T. Toda, H. Igarashi, M. Watanabe, J. Electrochem. Soc. 145 (1998) 4185–4188.
[171] M.K. Min, J.H. Cho, K.W. Cho, H. Kim, Electrochim. Acta 45 (2000) 4211–4217.
[172] M. Wakisaka, H. Suzuki, S. Mitsui, H. Uchida, M. Watanabe, J. Phys. Chem. C 112 (2008) 2750–2755.
[173] M. Wakisaka, H. Suzuki, S. Mitsui, H. Uchida, M. Watanabe, Langmuir 25 (2009) 1897–1900.
[174] F.T. Wagner, P.N. Ross, J. Electroanal. Chem. 250 (1988) 301–320.
[175] J. Clavilier, K. Elachi, A. Rodes, J. Electroanal. Chem. 272 (1989) 253–261.
[176] M. Kinne, T. Fuhrmann, J.F. Zhu, B. Trankenschuh, R. Denecke, H.P. Steinruck, Langmuir 20 (2004) 1819–1826.
[177] S. Koh, P. Strasser, J. Am. Chem. Soc. 129 (2007) 12624.
[178] R. Srivastava, P. Mani, N. Hahn, P. Strasser, Angew. Chem. Int. Ed. 46 (2007) 8988–8991.
[179] P. Mani, R. Srivastava, P. Strasser, J. Phys. Chem. C 112 (2008) 2770–2778.
[180] M. Mavrikakis, B. Hammer, J.K. Norskov, Phys. Rev. Lett. 81 (1998) 2819–2822.
[181] J.L. Zhang, M.B. Vukmirovic, Y. Xu, M. Mavrikakis, R.R. Adzic, Angew. Chem. Int. Ed. 44 (2005) 2132–2135.
[182] P. Strasser, S. Koha, J. Greeley, PCCP 10 (2008) 3670–3683.
[183] K.C. Neyerlin, R. Srivastava, C.F. Yu, P. Strasser, J. Power Sources 186 (2009) 261–267.
[184] V. Stamenkovic, B.S. Mun, K.J.J. Mayrhofer, P.N. Ross, N.M. Markovic, J. Rossmeisl, J. Greeley, J.K. Norskov, Angew. Chem. Int. Ed. 45 (2006) 2897–2901.
[185] N.M. Markovic, H.A. Gasteiger, P.N. Ross, J. Phys. Chem. 100 (1996) 6715–6721.
[186] N.M. Markovic, T.J. Schmidt, V. Stamenkovi, P.N. Ross, Fuel Cells 1 (2001) 105–116.
[187] J. Zagal, R.K. Sen, E. Yeager, J. Electroanal. Chem. 83 (1977) 207–213.
[188] A. Bettelheim, R. Parash, D. Ozer, J. Electrochem. Soc. 129 (1982) 2247–2250.
[189] J.P. Collman, I.M. Shiryaeva, R. Boulatov, Inorg. Chem. 42 (2003) 4807–4809.
[190] J.P. Collman, M. Kaplun, R.A. Decreau, Dalton Trans. (2006) 554–559.
[191] H. Alt, H. Binder, G. Sandsted, J. Catal. 28 (1973) 8–19.
[192] J.P. Collman, M. Marrocco, P. Denisevich, C. Koval, F.C. Anson, J. Electroanal. Chem. 101 (1979) 117–122.
[193] J.P. Collman, P.S. Wagenknecht, J.E. Hutchison, Angew. Chem. Int. Ed. 33 (1994) 1537–1554.
[194] J.P. Collman, R. Boulatov, C.J. Sunderland, L. Fu, Chem. Rev. 104 (2004) 561–588.
[195] J.P. Collman, P. Denisevich, Y. Konai, M. Marrocco, C. Koval, F.C. Anson, J. Am. Chem. Soc. 102 (1980) 6027–6036.
[196] J.E. Hutchison, T.A. Postlethwaite, R.W. Murray, Langmuir 9 (2002) 3277–3283.
[197] T.A. Postlethwaite, J.E. Hutchison, K.W. Hathcock, R.W. Murray, Langmuir 11 (2002) 4109–4116.
[198] C.W.B. Bezerra, L. Zhang, K.C. Lee, H.S. Liu, A.L.B. Marques, E.P. Marques, H.J. Wang, J.J. Zhang, Electrochim. Acta 53 (2008) 4937–4951.
[199] G. Faubert, G. Lalande, R. Cote, D. Guay, J.P. Dodelet, L.T. Weng, P. Bertrand, G. Denes, Electrochim. Acta 41 (1996) 1689–1701.
[200] E.B. Easton, A. Bonakdarpour, J.R. Dahn, Electrochem. Solid-State Lett. 9 (2006) A463–A467.
[201] E.B. Easton, A. Bonakdarpour, R. Yang, D.A. Stevens, J.R. Dahn, J. Electrochem. Soc. 155 (2008) B547–B557.
[202] A.D. Pauric, A.W. Pedersen, T. Andrusiak, E.B. Easton, J. Electrochem. Soc. 157 (2010) B370–B375.
[203] D. Villers, X. Jacques-Bedard, J.P. Dodelet, J. Electrochem. Soc. 151 (2004) A1507–A1515.
[204] M. Lefevre, E. Proietti, F. Jaouen, J.P. Dodelet, Science 324 (2009) 71–74.
[205] D. Chu, R.Z. Jiang, Solid State Ionics 148 (2002) 591–599.
[206] R.A. Bullen, T.C. Arnot, J.B. Lakeman, F.C. Walsh, Biosens. Bioelectron. 21 (2006) 2015–2045.
[207] P. Clauwaert, P. Aelterman, T.H. Pham, L. De Schamphelaire, M. Carballa, K. Rabaey, W. Verstraete, Appl. Microbiol. Biotechnol. 79 (2008) 901–913.
[208] A. Heller, PCCP 6 (2004) 209–216.
[209] Y. Liu, M.K. Wang, F. Zhao, Z.H. Guo, H.J. Chen, S.J. Dong, J. Electroanal. Chem. 581 (2005) 1–10.
[210] M.K. Wang, Y. Shen, Y. Liu, T. Wang, F. Zhao, B.F. Liu, S.J. Dong, J. Electroanal. Chem. 578 (2005) 121–127.
[211] H.J. Chen, Y.L. Wang, Y. Liu, Y.Z. Wang, L. Qi, S.J. Dong, Electrochem. Commun. 9 (2007) 469–474.
[212] D. Ivnitski, K. Artyushkova, P. Atanassov, Bioelectrochemistry 74 (2008) 101–110.
[213] D. Ivnitski, K. Artyushkova, R.A. Rincon, P. Atanassov, H.R. Luckarift, G.R. Johnson, Small 4 (2008) 357–364.
[214] S.J. You, Q.L. Zhao, J.N. Zhang, J.Q. Jiang, S.Q. Zhao, J. Power Sources 162 (2006) 1409–1415.
[215] Z. Li, X. Zhang, L. Lei, Process Biochem. 43 (2008) 1352–1358.
[216] M. Salmeron, R. Schlogl, Surf. Sci. Rep. 63 (2008) 169–199.
[217] G. Rupprechter, C. Weilach, J. Phys. Condens. Matter 20 (2008) 17.
[218] U. Gelius, B. Wannberg, P. Baltzer, H. Fellner-Feldegg, G. Carlsson, C.G. Johansson, J. Larsson, P. Münger, G. Vegerfors, J. Electron Spectrosc. Relat. Phenom. 52 (1990) 747–785.
[219] N. Martensson, P. Baltzer, P.A. Bruhwiler, J.O. Forsell, A. Nilsson, A. Stenborg, B. Wannberg, J. Electron. Spectrosc Relat. Phenom. 70 (1994) 117–128.
[220] T. Dutemeyer, C. Quitmann, M. Kitz, K. Dornemann, L.S.O. Johansson, B. Reihl, Rev. Sci. Instrum. 72 (2001) 2638–2648.
[221] M. Jacka, M. Kirk, M.M. El Gomati, M. Prutton, Rev. Sci. Instrum. 70 (1999) 2282–2287.
[222] F.H. Read, Rev. Sci. Instrum. 73 (2002) 1129–1139.
[223] L. Gori, R. Tommasini, G. Cautero, M. Barnaba, A. Accardo, S. Carrato, G. Paolucci, Nucl. Instrum. Methods Phys. Res., Sect. A 431 (1999) 338–346.

[224] L. Gregoratti, A. Barinov, E. Benfatto, G. Cautero, C. Fava, P. Lacovig, D. Lonza, M. Kiskinova, R. Tommasini, S. Mahl, W. Heichler, Rev. Sci. Instrum. 75 (2004) 64–68.
[225] T. Ohchi, S. Aoki, K. Sugisaki, J. Electron. Spectrosc Relat. Phenom. 80 (1996) 37–40.
[226] N. Yamaguchi, T. Ohchi, C. Fujikawa, A. Ogata, Y. Hisada, K. Okasaka, T. Hara, T. Tsunashima, Y. Iizuka, Rev. Sci. Instrum. 70 (1999) 1285–1287.
[227] B. Sonntag, Elsevier Science Bv, 2001, pp. 8–15.
[228] Z. Huang, R.D. Ruth, Phys. Rev. Lett. 80 (1998) 976.
[229] J. Giles, Nature 428 (2004) 789.